



LIS1 promotes the formation of activated cytoplasmic dynein-1 complexes

Zaw Min Htet^{1,2,6,9}, John P. Gillies^{1,3,9}, Richard W. Baker^{1,7}, Andres E. Leschziner^{1,4},
Morgan E. DeSantis^{1,8}✉ and Samara L. Reck-Peterson^{1,3,5}✉

Cytoplasmic dynein-1 is a molecular motor that drives nearly all minus-end-directed microtubule-based transport in human cells, performing functions that range from retrograde axonal transport to mitotic spindle assembly^{1,2}. Activated dynein complexes consist of one or two dynein dimers, the dynactin complex and an 'activating adaptor', and they show faster velocity when two dynein dimers are present³⁻⁶. Little is known about the assembly process of this massive ~4 MDa complex. Here, using purified recombinant human proteins, we uncover a role for the dynein-binding protein LIS1 in promoting the formation of activated dynein-dynactin complexes that contain two dynein dimers. Complexes activated by proteins representing three families of activating adaptors—BicD2, Hook3 and Ninl—all show enhanced motile properties in the presence of LIS1. Activated dynein complexes do not require sustained LIS1 binding for fast velocity. Using cryo-electron microscopy, we show that human LIS1 binds to dynein at two sites on the motor domain of dynein. Our research suggests that LIS1 binding at these sites functions in multiple stages of assembling the motile dynein-dynactin-activating adaptor complex.

Cytoplasmic dynein-1 (dynein) is responsible for the long-distance transport of nearly all cargos that move towards the minus ends of microtubules². Mutations in components of the dynein machinery cause neurodevelopmental and neurodegenerative diseases⁷. Activated human dynein is a large multisubunit complex that is composed of one or two dynein dimers (each dynein dimer contains two motor subunits and two copies each of five additional subunits), the dynactin complex (composed of 23 polypeptides) and a dimeric, coiled-coil-containing activating adaptor^{2-6,8} (Fig. 1a). The dynein motor subunit, or heavy chain, is an ATPase that contains six AAA+ domains and a microtubule-binding domain that emerges from a long coiled-coil stalk (Fig. 1b).

Although yeast dynein has the ability to move processively on its own *in vitro*⁹, mammalian dynein is largely immotile in the absence of dynactin and an activating adaptor^{3,4,10}. However, dynein activation *in vivo* is probably conserved across eukaryotes, as dynactin subunits and a candidate activating adaptor (Num1) are required for dynein function in yeast¹¹. Activating adaptors also link dynein-dynactin to its cargos^{2,8}. Nearly a dozen activating adaptors have been described; they share little sequence identity, but contain a long stretch of predicted coiled-coil that spans the ~40 nm length of

dynactin^{2,8}. All activated dynein complexes that have been investigated structurally can bind to two dynein dimers^{5,6} (Fig. 1a).

In the absence of these other components, mammalian dynein adopts a conformation known as Phi^{12,13}. Phi dynein is autoinhibited and cannot interact with microtubules productively¹². The current model for dynein activation proposes that Phi dynein must first adopt an 'open' conformation and ultimately a 'parallel' conformation that is observed when it is bound to dynactin and an activating adaptor^{5,6} (Fig. 1a). Little is known about how dynein switches between the autoinhibited Phi conformation and the open and parallel conformations that lead to the assembly of the motile activated dynein complex.

Genetic studies in model organisms place the dynein-binding protein LIS1 in the dynein pathway¹⁴⁻¹⁶. Given that deletion or mutations in LIS1 phenocopy deletion or mutation of dynein or dynactin subunits in these organisms¹⁴⁻¹⁶, LIS1 is considered to be a positive regulator of the cellular activities of dynein. Activities that require LIS1 range from organelle trafficking¹⁷⁻²⁰ to nuclear migration/positioning^{15,21-23} to RNA localization²⁴. LIS1 is mutated in the neurodevelopmental disease type-1 lissencephaly²⁵, and was first directly linked to dynein through genetic studies in *Aspergillus nidulans*¹⁵. LIS1 is a dimer of β -propellers^{26,27} and yeast LIS1 binds to dynein at two distinct sites on the dynein motor domain—the ATPase ring of dynein at AAA3 and AAA4 (site_{ring}) and dynein's stalk²⁸⁻³⁰ (site_{stalk}; Fig. 1b). In yeast, binding of LIS1 to dynein at site_{ring} is correlated with tight microtubule binding and decreased velocity^{29,30}, whereas binding at both sites correlates with weak microtubule binding and increased velocity³⁰. LIS1 also increases the binding of mammalian dynein to microtubules^{31,32} and increases the velocity of mammalian dynein-dynactin complexes that contain the BicD2-activating adaptor^{33,34}. How LIS1 exerts these effects on mammalian dynein is unknown. It is also unknown whether LIS1 has the same effects on dynein-dynactin bound to other activating adaptors.

To determine how LIS1 regulates activated human dynein complexes, we purified full-length recombinant human dynein in the presence of its accessory chains (dynein)³ and human LIS1 from insect cells, dynactin from human HEK293T cells³⁵ and the human activating adaptors BicD2, Hook3 and Ninl from *Escherichia coli* (Extended Data Fig. 1a). As some activating adaptors are known to be autoinhibited³⁶, we used well-characterized carboxy-terminal truncations of BicD2, Hook3 and Ninl^{3,4,35} (Fig. 1c). We generated

¹Department of Cellular and Molecular Medicine, University of California San Diego, La Jolla, CA, USA. ²Biophysics Graduate Program, Harvard Medical School, Boston, MA, USA. ³Division of Biological Sciences, Cell and Developmental Biology Section, University of California San Diego, La Jolla, CA, USA.

⁴Division of Biological Sciences, Molecular Biology Section, University of California San Diego, La Jolla, CA, USA. ⁵Howard Hughes Medical Institute, Chevy Chase, MD, USA. ⁶Present address: Department of Molecular and Cell Biology, University of California Berkeley, Berkeley, CA, USA. ⁷Present address: Department of Biochemistry and Biophysics, University of North Carolina, Chapel Hill, NC, USA. ⁸Present address: Department of Molecular, Cellular and Developmental Biology, University of Michigan, Ann Arbor, MI, USA. ⁹These authors contributed equally: Zaw Min Htet, John P. Gillies.

✉e-mail: mdesant@umich.edu; sreckpeterson@ucsd.edu

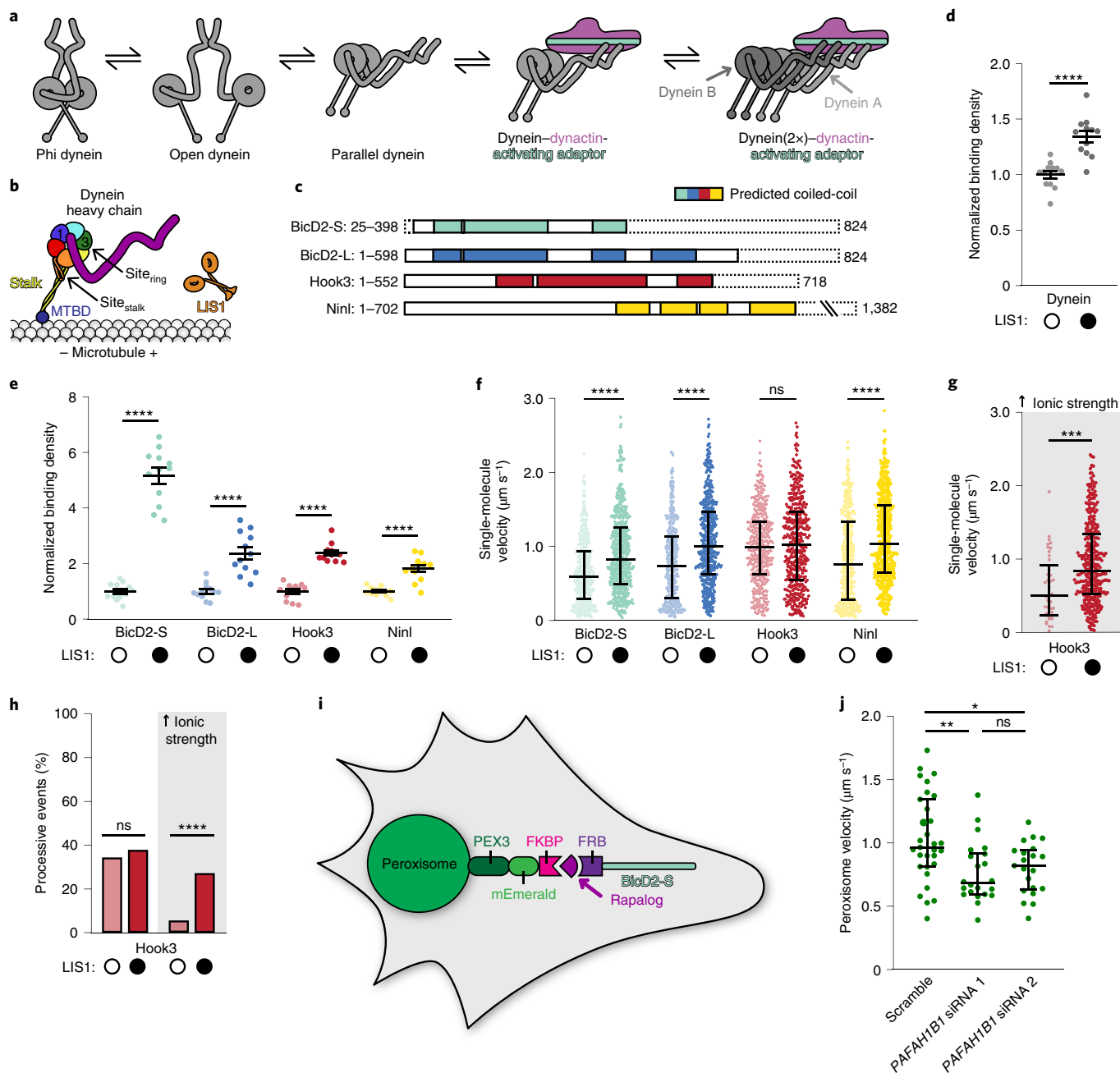


Fig. 1 | LIS1 increases microtubule binding and velocity of activated dynein complexes. **a**, The current model for dynein activation. Dynein is autoinhibited in the Phi conformation, opens, and then adopts a parallel conformation in the activated dynein complex, which can contain two dynein dimers (A and B). **b**, Schematic of the AAA+ ATPase dynein heavy chain. The two LIS1-binding sites, site_{ring} and site_{stalk} are shown. MTBD, microtubule binding domain. **c**, The activating adaptor constructs used in this study. The dashed lines indicate the regions that were truncated. **d, e**, Binding density of full-length recombinant human dynein with its associated intermediate, light-intermediate and light chains (**d**) or dynein-dynactin-activating adaptor complexes (**e**) on microtubules in the absence (white circles) or presence (black circles) of 300 nM LIS1. Data were normalized to a density of 1.0 in the absence of LIS1. Data are mean ± s.e.m.; *****P* < 0.0001. **f**, Single-molecule velocity of dynein-dynactin-activating adaptor complexes in the absence (white circles) or presence (black circles) of 300 nM LIS1. Data are median ± interquartile range. *****P* < 0.0001; ns, *P* = 0.3498. **g**, Single-molecule velocity of dynein-dynactin-Hook3 complexes in a higher-ionic-strength buffer (67.5 mM compared with 37.5 mM in our standard buffer) in the absence (white circle) or presence (black circle) of 300 nM LIS1. Data are median ± interquartile range. ****P* = 0.0004. **h**, Percentage of processive runs of dynein-dynactin-Hook3 complexes in standard and higher (grey) ionic-strength motility buffer in the absence (white circles) or presence (black circles) of 300 nM LIS1. Statistical analysis was performed on data pooled from all replicates using χ^2 tests. *****P* < 0.0001; ns, *P* = 0.0724. **i**, Peroxisome relocation assay. The peroxisomal protein, Pex3, was fused to mEmerald and FKBP, whereas BicD2-S was fused to FRB. Rapalog induces the association of FKBP and FRB. **j**, Peroxisome velocity in human U2OS cells with scrambled or *PAFAH1B1* siRNA knockdown with two independent siRNAs. Data are median ± interquartile range. ***P* = 0.0071; **P* = 0.0464; ns, *P* > 0.9999. Source data are available online.

two truncations of BicD2 as follows: BicD2-S (amino acids 25–398), which activates dynein *in vitro*^{3,4}, and BicD2-L (amino acids 1–598), which activates dynein in cells^{18,37}.

We first determined the effects of LIS1 on the microtubule-binding properties of dynein alone and dynein–dynactin bound to different activating adaptors using a single-molecule assay³⁰. LIS1 increased

the microtubule-binding density of dynein alone (Fig. 1d, Extended Data Fig. 1b), consistent with studies of yeast^{29,30} and mammalian^{31,32} dynein. LIS1 also increased the microtubule-binding density of dynein–dynactin complexes bound by the activating adaptors BicD2-S, BicD2-L, Hook3 and Ninl (Fig. 1e, Extended Data Fig. 1b).

Next, we examined how LIS1 affected the motile properties of activated dynein complexes. Although LIS1 inhibits the motility of human dynein alone in microtubule gliding assays^{31,33,38,39}, in agreement with some previous studies^{33,34}, we found that LIS1 increased the velocity of dynein–dynactin–BicD2-S complexes (Fig. 1f, Extended Data Fig. 1c, Supplementary Video 1). We also found that LIS1 increased the velocity of dynein–dynactin activated by BicD2-L and Ninl in our standard motility assay buffer (Fig. 1f, Extended Data Fig. 1c, Supplementary Videos 2–4). LIS1 also increased the percentage of processive runs for dynein–dynactin activated by BicD2-S, BicD2-L and Ninl (Extended Data Fig. 1d). Although Hook3-activated dynein complexes were not affected by LIS1 in these conditions (Fig. 1f), increasing the ionic strength of our assay buffer led to increased velocity and an increase in processive runs of these complexes in the presence of LIS1 (Fig. 1g,h, Supplementary Video 5). We interpret this difference in sensitivity to the ionic strength of our assay conditions as an indication that Hook3 may have a higher affinity for dynactin, the dynein tails or the dynein light-intermediate chains compared with BicD2 and Ninl. These data show that LIS1 increases both microtubule binding and motility of dynein–dynactin complexes bound by activating adaptors from three different families and allude to a role for LIS1 in activated dynein–dynactin complex formation.

We next investigated whether LIS1 has a similar effect on dynein velocity in cells, using a well-established peroxisome-relocation assay^{37,40} (Fig. 1i). We co-transfected human U2OS cells with (1) the rapamycin-binding protein FRB fused to BicD2-S and (2) another rapamycin-binding protein FKBP fused to mEmerald and the peroxisome-targeting protein Pex3 (Fig. 1i). In U2OS cells, peroxisomes rarely move, but after the addition of rapalog—which causes FRB and FKBP to interact—we observed many processive runs. This is an indication that BicD2-S recruits and activates dynein–dynactin⁴⁰ (Supplementary Videos 6–9). We observed a significant decrease in peroxisome velocity when *PAFAH1B1* (which encodes LIS1) expression was knocked down using short interfering RNA (siRNA; Fig. 1j, Extended Data Fig. 1e–g), suggesting that LIS1 also increases the velocity of dynein complexes in a cellular environment.

We next sought to determine where LIS1 binds to human dynein. Experiments with yeast proteins showed that LIS1 binds to dynein at two sites on the dynein motor domain (site_{ring} and site_{stalk})^{29,30}, although previous studies using mammalian protein fragments reported interactions with other regions of dynein^{41,42}. We used cryo-electron microscopy (cryo-EM) to identify the LIS1-binding sites on human dynein. We purified monomeric human dynein motor domains and mixed them with dimeric human LIS1 in the presence of ATP-vanadate. This ATP analogue was previously shown to promote an interaction between mammalian dynein and LIS1 (ref. 32) and causes dynein's linker to adopt a bent position⁴³ that would prevent the linker from sterically interfering with LIS1 binding at site_{ring}. We generated two-dimensional (2D) class averages of the dynein–LIS1 complex that showed high-resolution features in both dynein and LIS1 (Fig. 2a).

To determine whether the binding sites for LIS1 are similar in human and yeast dynein, we compared our experimental class averages with calculated 2D projections of a model of human dynein bound to LIS1 (Fig. 2b). To generate this model, we combined the structure of human dynein-2 bound to ATP-vanadate (PDB, 4RH7)⁴⁴ with a homology model of human LIS1 bound to dynein at the two binding sites observed with the yeast proteins (PDB, 5VLJ)³⁰ (Fig. 2b). To highlight the densities that correspond to

LIS1, we also calculated 2D projections of human dynein-2 alone (Fig. 2c). The correspondence between our data and the model with two LIS1 molecules bound (Fig. 2a,b) suggests that the yeast and human LIS1-binding sites are in similar regions of the dynein motor domain, on the ring at AAA3/4 and on the stalk. The strong preferred orientation adopted by the sample prevented us from obtaining a 3D reconstruction and mapping the exact sites of interaction onto either human dynein or LIS1. The stoichiometry of this complex is 1 dynein monomer to 1.2 ± 0.3 LIS1 dimers (Extended Data Fig. 2a), suggesting that the majority of dynein monomers are bound to a single LIS1 dimer.

Mutation of five amino acids on the dynein-binding face of yeast LIS1 disrupts its interaction with dynein²⁸. We generated the equivalent mutations in human LIS1 (LIS1-5A; Fig. 2d). To determine whether LIS1-5A can enhance the velocity of activated dynein complexes, we focused on complexes that are activated by BicD2-S, as LIS1 had the greatest effect on these complexes (Fig. 1g). We found that 300 nM LIS1-5A still enhanced the velocity of dynein–dynactin–BicD2-S complexes. We hypothesized that LIS1-5A might still weakly interact with dynein. We therefore lowered the concentration of LIS1 and LIS1-5A to 24 nM; under these conditions, wild-type (WT) LIS1 more potently increased dynein velocity compared with LIS1-5A (Fig. 2e, Extended Data Fig. 2b). We also found that LIS1-5A was less potent at enhancing processive runs of dynein–dynactin–Hook3 complexes compared with WT LIS1 in a higher-ionic-strength buffer (Fig. 2f), and the velocity of these runs was no longer increased (Extended Data Fig. 2c,d).

As LIS1 is a dimer, we wondered whether the effects of LIS1 on activated dynein–dynactin complexes required dimerization. To test this, we purified human LIS1 lacking its amino-terminal high-affinity LisH dimerization domain²⁶, which we refer to as LIS1ΔN. Similar to the equivalent yeast construct, which is a monomer by gel filtration analysis²⁹, the human construct is mostly monomeric (Extended Data Fig. 2e). However, using the human construct, a small amount of dimer was also observed (Extended Data Fig. 2e), probably due to an interaction between the two β-propellers of LIS1, as observed here and previously³⁰ using Cryo-EM. LIS1ΔN still increased dynein–dynactin–BicD2-S velocity at the same molar ratio of dynein to LIS1 β-propellers (Fig. 2g), indicating that the high-affinity LisH dimerization domain is not required for LIS1 to increase the velocity of dynein.

As activated dynein complexes containing two dynein dimers are faster than those containing a single dynein dimer³, we hypothesized that LIS1 may have a role in promoting the recruitment of a second dynein dimer to the dynein–dynactin complex. To determine whether LIS1 enhances the formation of dynein–dynactin complexes in vitro, we measured the formation of activated dynein complexes by mixing dynein and dynactin with an excess of BicD2-S conjugated to magnetic beads. We then quantified the percentage of dynein bound to the BicD2-S beads (Fig. 3a). The presence of LIS1 increased the percentage of dynein that was bound to BicD2-S beads (Fig. 3b) and dynactin was required for this effect (Fig. 3c).

To directly test whether LIS1 promotes the recruitment of a second dynein dimer to the activated complex, we performed two-colour single-molecule assays. To do this, we added equimolar amounts of dynein labelled with either TMR or Alexa647 to dynactin and BicD2-S and quantified the percentage of moving two-colour complexes. If all of the moving dynein complexes contained two dynein dimers, 50% of events would show co-localization (Fig. 3d). The presence of LIS1 significantly increased the number of moving two-colour dynein–dynactin–BicD2-S complexes (Fig. 3e,f). Two-colour complexes moved faster in both the presence and absence of LIS1 (Extended Data Fig. 3a). One-colour complexes in the presence of LIS1 also moved faster, presumably because half of these events contained two dynein dimers labelled with the same colour (Extended Data Fig. 3a).

We conclude that LIS1 promotes the recruitment of a second dynein dimer to activated dynein complexes.

We wondered whether LIS1 must remain bound to moving activated dynein complexes to sustain fast velocity. To address this, we sought to determine whether TMR-labelled LIS1 co-migrated with moving dynein–dynactin–BicD2-S complexes tagged with Alexa647. Most of our earlier experiments used 300 nM LIS1, a concentration that is too high to visualize single LIS1 molecules. We therefore lowered the LIS1 concentration to 50 nM, which is still well above the concentration at which a maximal increase in dynein velocity by LIS1 is observed (Fig. 4a, Extended Data Fig. 2b). Single-molecule motility assays with TMR–LIS1 and Alexa647–dynein–dynactin–BicD2-S complexes showed that only $16.8 \pm 1.9\%$ of dynein runs co-migrated with LIS1, with co-migrating runs moving slower than those with no detectable LIS1 (Fig. 4b,c). Occasionally, the disappearance of the TMR–LIS1 signal coincided with an increase in speed of a dynein–dynactin–BicD2-S run (Fig. 4d), similar to a previous report³⁴. As shown previously³², we found that human LIS1 in the absence of dynein does not bind to microtubules (Extended Data Fig. 4a), suggesting that the effects of LIS1 on dynein activity and complex assembly that we observed are not due to an interaction between LIS1 and microtubules. We also found that LIS1-5A increased the velocity of activated dynein complexes significantly less than WT LIS1 (Extended Data Fig. 4b) and we observed no colocalization of TMR–LIS1-5A with Alexa647–dynein (Extended Data Fig. 4c). These results suggest that the presence of LIS1 is not required for sustained fast velocity of activated dynein complexes. Our results that show that activated dynein complexes move faster when LIS1 is no longer co-migrating are consistent with contemporaneous research⁴⁵, but differ from other reports^{33,34}, perhaps due to differences in assay conditions or protein source.

We next investigated which step(s) that LIS1 affects in the dynein-complex-assembly pathway (Fig. 1a). As the $\text{site}_{\text{ring}}$ LIS1-binding site on dynein is not accessible in Phi dynein (Fig. 5a), we wondered whether LIS1 had higher affinity for a dynein mutant that does not form the Phi particle (K1610E and R1567E¹², ‘open dynein’). Indeed, we found that LIS1 had a higher affinity for open dynein (Fig. 5b). We hypothesize that binding of LIS1 to dynein at

$\text{site}_{\text{ring}}$ alters the equilibrium between Phi and open dynein to favour the open conformation.

We next considered two possibilities. First, that the only role of LIS1 is to stabilize dynein’s open conformation; and second, that—in addition to this role—LIS1 also promotes activated complex formation. To do this we examined open dynein complexes in the absence of LIS1 and found that open dynein–dynactin–BicD2-S complexes were more likely to form and moved faster compared with complexes containing WT dynein¹² (Fig. 5c,d). We then investigated whether LIS1 altered the motile properties of complexes containing open dynein. We found that LIS1 further increased complex formation and velocity of open dynein–dynactin–BicD2-S complexes (Fig. 5d). LIS1 also increased the percentage of complexes containing two dynein dimers when open dynein was used (Fig. 5e). Previous studies showed that the open dynein mutant does not

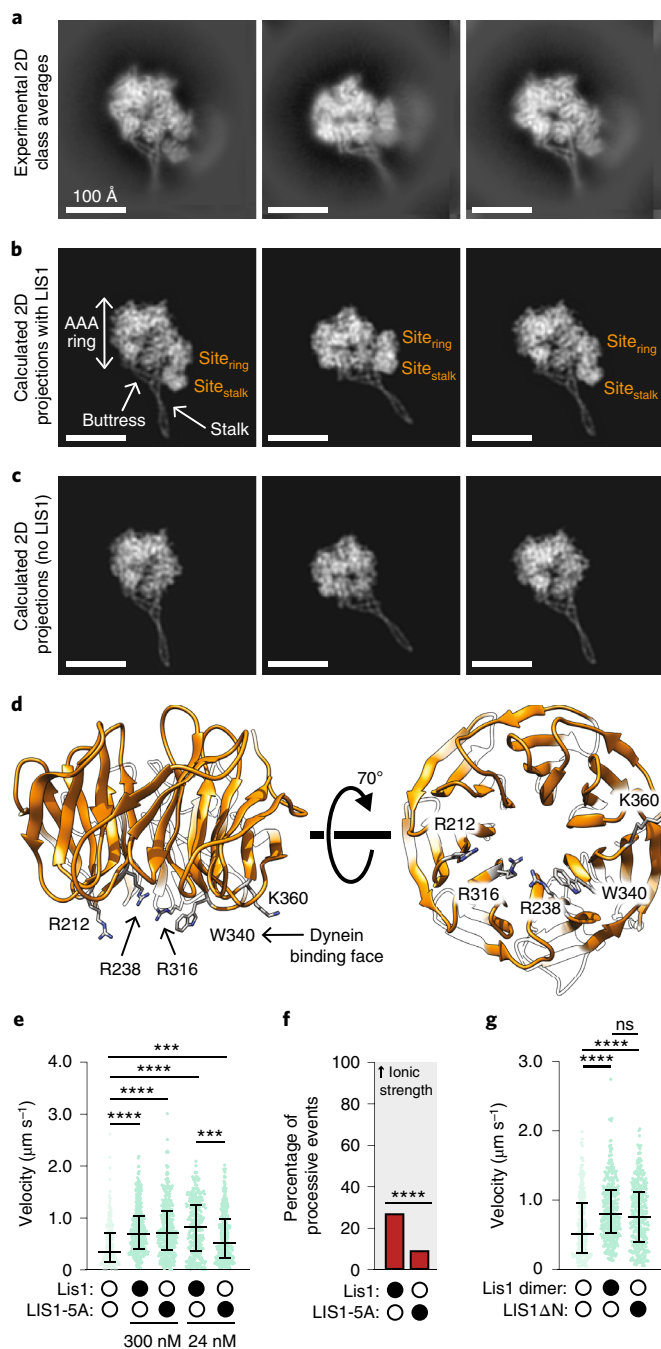


Fig. 2 | Human LIS1 binds to the human dynein motor domain at AAA3/4 and the stalk. a, 2D class averages of human dynein monomers bound to human LIS1 dimers in the presence of ATP-vanadate. Scale bars, 100 Å.

b, Best-matching projections of a model combining human dynein-2 bound to ATP-vanadate (PDB 4RH7) with homology models of human LIS1 at the locations at which LIS1 binds to yeast dynein in the presence of ATP-vanadate (PDB 5VLJ). The two LIS1-binding sites ($\text{site}_{\text{ring}}$ and $\text{site}_{\text{stalk}}$) identified in yeast dynein, as well as dynein’s AAA ring, stalk and buttress, are labelled. Scale bars, 100 Å. **c**, Projections of human dynein-2 in the presence of ATP-vanadate (PDB 4RH7) alone in the same orientations as those shown in **b**. Scale bars, 100 Å. **d**, Homology model of human LIS1 (from SWISS-MODEL) showing the five residues mutated to alanine in LIS1-5A. **e**, Single-molecule velocity of dynein–dynactin–BicD2-S complexes in the absence (white circles) or presence (black circles) of 300 nM or 24 nM LIS1 or LIS1-5A. Data are median \pm interquartile range. **** $P < 0.0001$; *** $P = 0.0002$. **f**, The percentage of processive runs of dynein–dynactin–Hook3 complexes in a higher-ionic-strength buffer in the absence (white circles) or presence (black circles) of 300 nM LIS1 or LIS1-5A. Data in the presence of 300 nM LIS1 are also shown in Fig. 1h. Statistical analysis was performed on data pooled from all replicates using χ^2 tests. **** $P < 0.0001$. **g**, Single-molecule velocity of dynein–dynactin–BicD2-S complexes in the absence (white circles) or presence (black circles) of 300 nM LIS1 dimer or 600 nM LIS1 Δ N. As LIS1 Δ N is largely monomeric (Extended Data Fig. 2e), 300 nM LIS1 dimer is roughly equivalent to 600 nM LIS1 Δ N. Data are median \pm interquartile range. **** $P < 0.0001$; ns, $P = 0.0906$. Source data are available online.

**** $P < 0.0001$; *** $P = 0.0002$. **f**, The percentage of processive runs of dynein–dynactin–Hook3 complexes in a higher-ionic-strength buffer in the absence (white circles) or presence (black circles) of 300 nM LIS1 or LIS1-5A. Data in the presence of 300 nM LIS1 are also shown in Fig. 1h. Statistical analysis was performed on data pooled from all replicates using χ^2 tests. **** $P < 0.0001$. **g**, Single-molecule velocity of dynein–dynactin–BicD2-S complexes in the absence (white circles) or presence (black circles) of 300 nM LIS1 dimer or 600 nM LIS1 Δ N. As LIS1 Δ N is largely monomeric (Extended Data Fig. 2e), 300 nM LIS1 dimer is roughly equivalent to 600 nM LIS1 Δ N. Data are median \pm interquartile range. **** $P < 0.0001$; ns, $P = 0.0906$. Source data are available online.

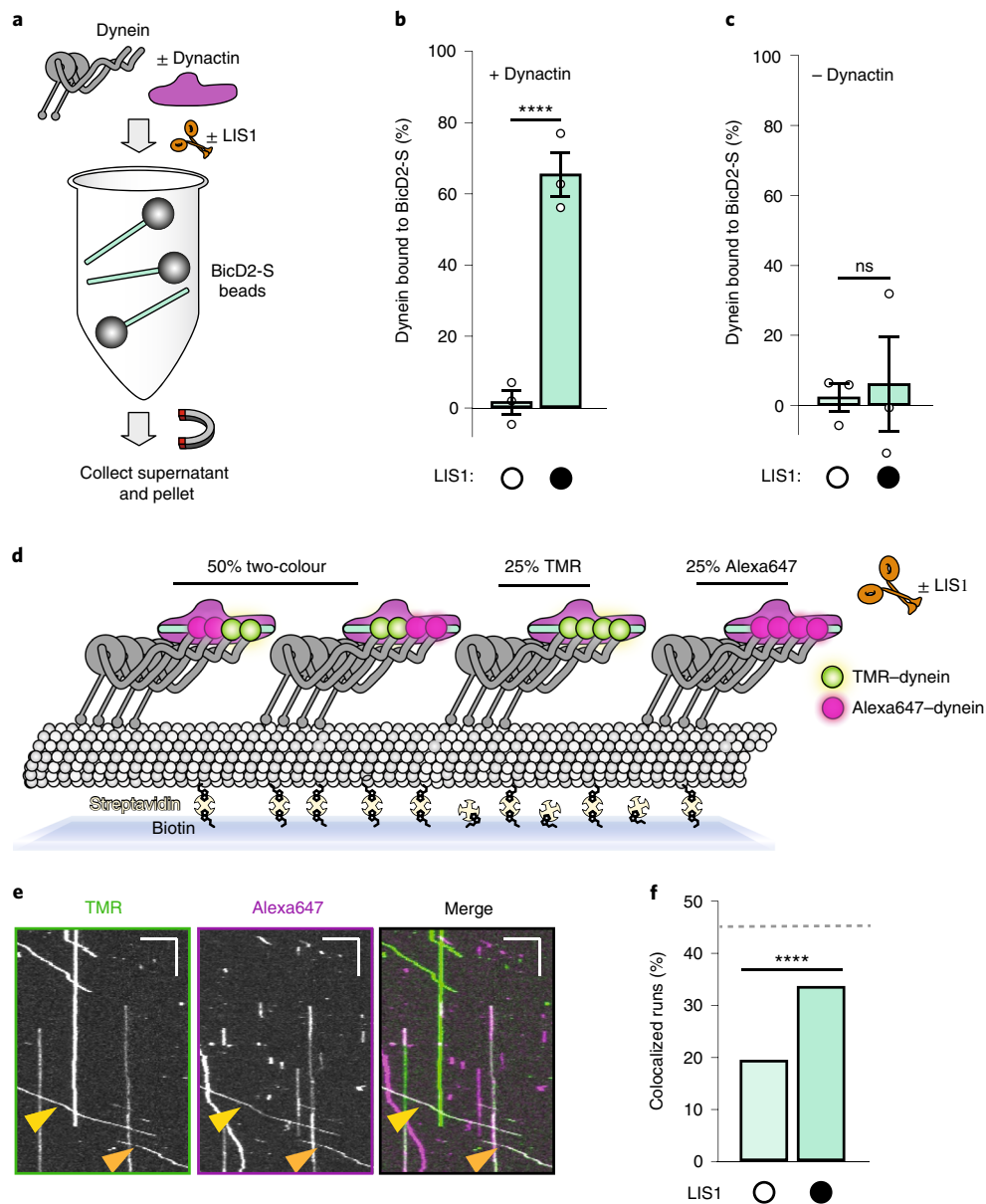


Fig. 3 | LIS1 recruits a second dynein dimer to dynein-dynactin-BicD2-S complexes. **a**, Schematic of the dynein-dynactin complex-formation assay. **b,c**, The percentage of dynein bound to BicD2-S-coupled beads in the presence (**b**) or absence (**c**) of dynactin and in the absence (white circle) or presence (black circle) of 150 nM LIS1. Data are mean \pm s.e.m. **** $P < 0.0001$; ns, $P = 0.8026$. **d**, Schematic of the maximum probability of forming various dynein-dynactin-BicD2-S complexes containing two dynein dimers. The maximum probability of colocalization was 45% (grey dashed line shown in **f**) given our labelling efficiency (see Methods). **e**, Representative kymographs of the colocalization of TMR- and Alexa647-labelled dynein in moving dynein-dynactin-BicD2-S complexes in the presence of 300 nM LIS1. Each channel is shown separately (left and middle) and the merged TMR and Alexa647 channels are shown in pseudocolour (right). Scale bars, 10 μm (x) and 20 s (y). Data are quantified in **f**. **f**, The percentage of two-colour dynein-dynactin-BicD2-S runs in the absence (white circle) or presence (black circle) of 300 nM LIS1. Statistical analysis was performed using χ^2 tests. **** $P < 0.0001$. Source data are available online.

form Phi particles¹². Assuming that this is the case in our experiments, the ability of LIS1 to further activate open dynein suggests that the effect of LIS1 on complex formation may have additional roles beyond altering the equilibrium between Phi and open dynein.

Together, our research suggests that LIS1 promotes the formation of human dynein-dynactin-activating adaptor complexes that contain two dynein dimers. Experiments in human cells¹⁸, *Drosophila* embryos²⁴, *Xenopus* extracts³⁹, *A. nidulans*⁴⁶ and yeast⁴⁷ showed that LIS1 is required for the interactions of dynein and dynactin with each other and/or with their cargos. Our research offers a biochemical

explanation for this requirement for LIS1. Our data suggest that LIS1 promotes complex formation by favouring a conformation of dynein that drives association with dynactin and an activating adaptor. First, LIS1 may promote the open dynein conformation (Fig. 5f, i). We propose this on the basis of our data showing that open dynein has a higher affinity for LIS1 and because the structure of Phi dynein is incompatible with LIS1 binding at site_{ring}. Recent research in *A. nidulans*⁴⁶ and *Saccharomyces cerevisiae*⁴⁷ also supports this. Second, LIS1 may favour a conformation of dynein that is primed to assemble the fully activated complex (Fig. 5f, ii).

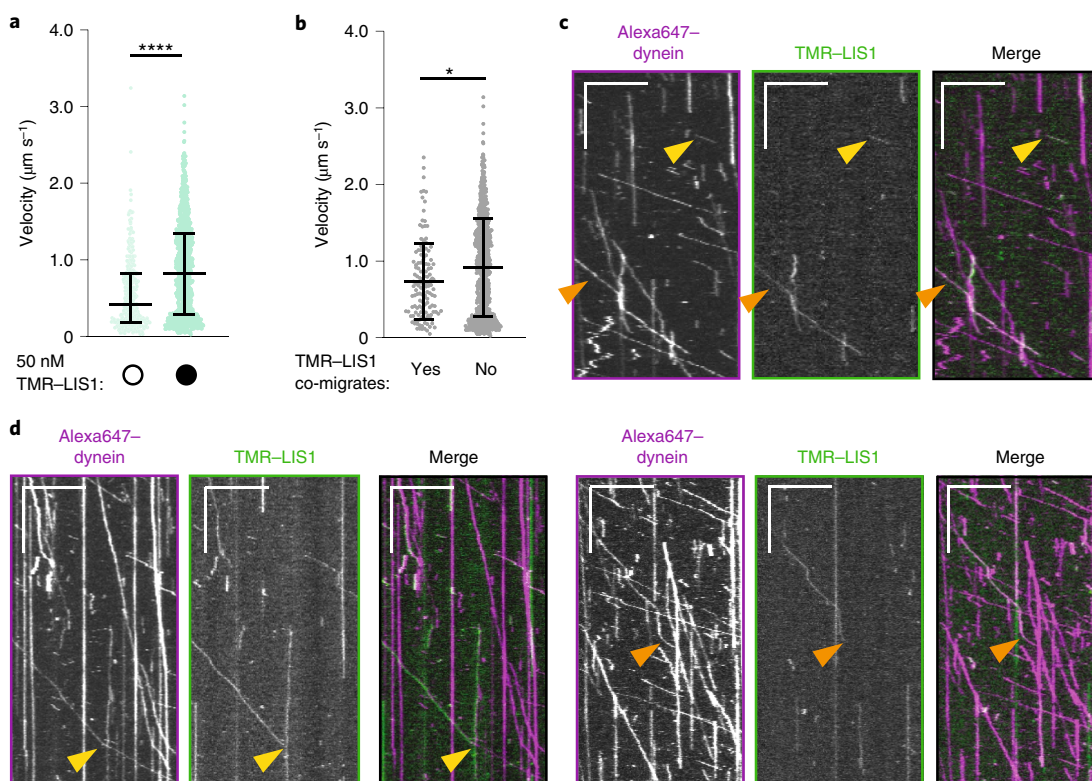


Fig. 4 | LIS1 is not required to sustain the fast velocity of activated dynein complexes. **a**, Single-molecule velocity of dynein–dynactin–BicD2–S complexes in the absence (white circle) or presence (black circle) of 50 nM TMR–LIS1. Data are median \pm interquartile range. **** $P < 0.0001$. **b**, Single-molecule velocity of Alexa647–dynein–dynactin–BicD2–S complexes in the presence of 50 nM TMR–LIS1, either co-migrating with TMR–LIS1 (yes) or not (no). Data are median \pm interquartile range. * $P = 0.0011$. **c**, Representative kymographs of the Alexa647–dynein and TMR–LIS1 channels (left and middle) and the merged images in pseudocolour (right). The arrowheads indicate colocalized runs. Scale bars, 10 μm (x) and 20 s (y). Data are quantified in **b**. **d**, Kymographs showing examples of dynein’s velocity changing after loss of the TMR–LIS1 signal. The Alexa647–dynein and TMR–LIS1 channels are shown (left and middle) and the merged images in pseudocolour (right). The arrowheads indicate instances of velocity change. Four such events were observed. Scale bars, 10 μm (x) and 20 s (y). Data are quantified in **b**. Source data are available online.

Our data showing that open dynein is further activated by LIS1 support this. Third, LIS1 favours the formation of dynein complexes that contain two dynein dimers, which move faster (Fig. 5f, iii). Our single-molecule experiments measuring the velocity of activated dynein complexes in the presence of LIS1 and our experiments showing that LIS1 promotes the recruitment of two dynein dimers support this. As we also observe these effects with LIS1 ΔN , the underlying mechanism does not rely on the high-affinity LIS1H dimerization domain, although interactions between the LIS1 β -propellers could have a role. Finally, once a fully activated dynein–dynactin-activating adaptor complex is formed, LIS1 dissociates from moving complexes (Fig. 5f, iv). This component of our model is based on our data showing that most moving dynein complexes do not remain bound to LIS1 and, those that do, move slower. Complementary findings were obtained in contemporaneous research that support steps (iii) and (iv) of our model⁴⁵.

How does this research, as well as other recent studies^{45–47}, relate to previous mechanistic studies of yeast LIS1 that showed how allosteric effects of LIS1 binding to the motor domain of dynein controlled the microtubule binding affinity of dynein^{28–30}? Earlier studies in yeast were performed in the absence of dynactin and an activating adaptor because yeast dynein is a processive motor on its own⁹, enabling the dissection of dynein function in a minimal system (however, dynactin and a candidate activating adaptor, Num1, are required for yeast dynein function in vivo). Here we show that human LIS1 binds to two sites on the motor domain of human

dynein that are similar to the yeast binding sites^{28–30}. Vertebrate LIS1 increases the affinity of dynein for microtubules and slows microtubule gliding velocity^{31–33,39}, again mirroring findings in yeast. Thus, the LIS1 binding sites on dynein and some of the consequences of these interactions on dynein’s mechanochemical cycle are conserved.

The ability of LIS1 to regulate dynein’s mechanochemistry may be important for its role in assembling activated dynein complexes. For example, dynein idling on the microtubule (caused by tight microtubule binding induced by LIS1) could be well suited for helping with the challenging kinetics of loading two dynein motors onto dynactin before transport begins. In support of this, LIS1 has a role in localizing dynein to microtubule plus ends^{21,48} or initiating transport from microtubule plus ends^{19,20,49}, where tight microtubule binding and reduced motility could be important for maintaining dynein at these sites. Binding of LIS1 to dynein at microtubule plus ends could promote the open dynein conformation, lead to tight microtubule binding of dynein and, ultimately, favour the formation of activated dynein–dynactin-activating adaptor complexes that contain two dynein dimers. LIS1 binding to dynein may have additional allosteric effects that promote the formation of the full activated dynein–dynactin complex, perhaps influencing the conformation of the dynein tails that interact with dynactin and activating adaptors. A contemporaneous study suggests that regulation of yeast dynein by LIS1 involves an interaction between LIS1 and microtubules⁴⁷. However, much of the past research with yeast proteins^{28–30} cannot be accounted for by this model. Furthermore, we

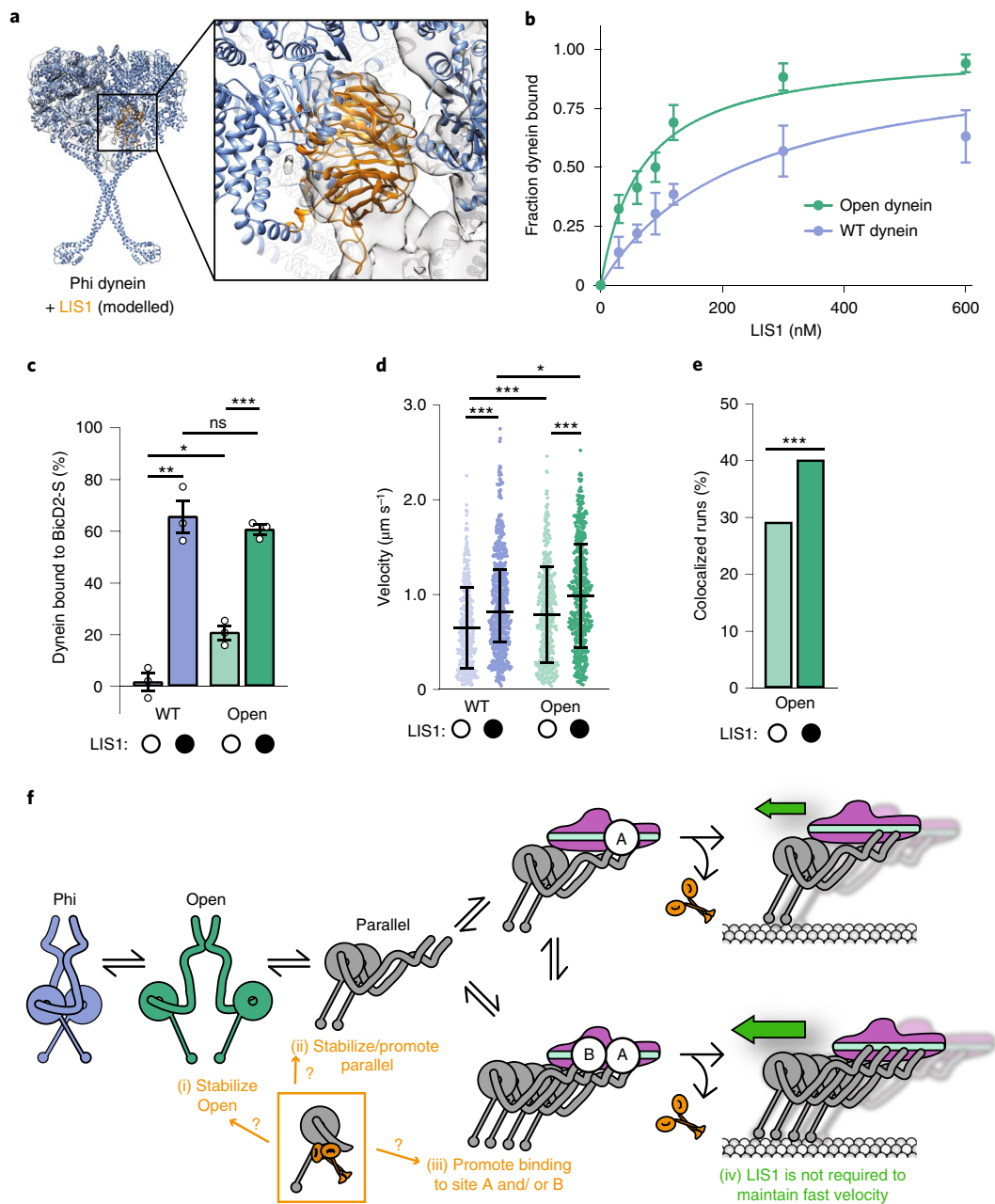


Fig. 5 | LIS1 preferentially binds to open dynein and enhances the formation of complexes containing two open dynein dimers. **a**, One of the dynein protomers in the Phi conformation (PDB 5NVU) was aligned to the structure of yeast dynein (AAA3-Walker B) bound to LIS1 in the presence of ATP-vanadate (PDB 5VLJ). The inset shows the cryo-EM map for the yeast structure with LIS1 docked at site_{ring} and highlights the steric incompatibility between the Phi conformation and binding of LIS1 at this site. **b**, Determination of the binding affinity of LIS1 for WT dynein (blue, $K_d = 144 \pm 25$ nM) and open dynein (green, $K_d = 80 \pm 8.1$ nM). **c**, The percentage of WT dynein (blue) and open dynein (green) bound to BicD2-S conjugated to beads in the absence (white circles) or presence (black circles) of 150 nM LIS1. Data are mean \pm s.e.m. Data with WT dynein in the presence and absence of LIS1 are also shown in Fig. 3b. Statistical analysis was performed using two-tailed unpaired *t*-tests with Bonferroni-corrected significance levels for two comparisons. *** $P = 0.0003$; ** $P = 0.0008$; * $P = 0.0118$; ns, $P = 0.4857$. **d**, Single-molecule velocity of dynein-dynactin-BicD2-S complexes with WT dynein (blue) and open dynein (green) in the absence (white circles) or presence (black circles) of 300 nM LIS1. Data are median \pm interquartile range. *** $P < 0.0001$; * $P = 0.0241$. Data with WT dynein with and without LIS1 are also shown in Fig. 1f. **e**, The percentage of two-colour colocalized runs with activated dynein complexes with open dynein in the absence (white circle) or presence (black circle) of 300 nM LIS1. Statistical analysis was performed using χ^2 tests. *** $P = 0.0010$. The labelling efficiency for both TMR-dynein and Alexa647-dynein in this experiment was 100%. **f**, Model of the roles of LIS1 in forming activated dynein complexes. Source data are available online.

and others³² have shown that mammalian LIS1 does not interact with microtubules.

Finally, we have shown that proteins representing three distinct families of activating adaptors, BicD2, Hook3 and Ninl, all move

faster in the presence of LIS1. This raises the possibility that activated dynein complexes in cells contain two dynein dimers. We hypothesize that related activating adaptors or candidate activating adaptors will also use LIS1 to form activated complexes. In humans

there are additional BicD, Hook and Ninl family members, as well as a number of known and candidate activating adaptors^{2,8}. Thus, we predict that LIS1 has a role in the cell biological processes that additional dynein activating adaptors facilitate.

Online content

Any methods, additional references, Nature Research reporting summaries, source data, extended data, supplementary information, acknowledgements, peer review information; details of author contributions and competing interests; and statements of data and code availability are available at <https://doi.org/10.1038/s41556-020-0506-z>.

Received: 16 April 2019; Accepted: 11 March 2020;

Published online: 27 April 2020

References

- Raaijmakers, J. A. & Medema, R. H. Function and regulation of dynein in mitotic chromosome segregation. *Chromosoma* **123**, 407–422 (2014).
- Reck-Peterson, S. L., Redwine, W. B., Vale, R. D. & Carter, A. P. The cytoplasmic dynein transport machinery and its many cargoes. *Nat. Rev. Mol. Cell Biol.* **19**, 382–398 (2018).
- Schlager, M. A., Hoang, H. T., Urnavicius, L., Bullock, S. L. & Carter, A. P. In vitro reconstitution of a highly processive recombinant human dynein complex. *EMBO J.* **33**, 1855–1868 (2014).
- Mckenney, R. J., Huynh, W., Tanenbaum, M. E., Bhabha, G. & Vale, R. D. Activation of cytoplasmic dynein motility by dynactin-cargo adapter complexes. *Science* **345**, 337–341 (2014).
- Urnavicius, L. et al. Cryo-EM shows how dynactin recruits two dyneins for faster movement. *Nature* **554**, 202–206 (2018).
- Grotjahn, D. A. et al. Cryo-electron tomography reveals that dynactin recruits a team of dyneins for processive motility. *Nat. Struct. Mol. Biol.* **25**, 203–207 (2018).
- Lipka, J., Kuijpers, M., Jaworski, J. & Hoogenraad, C. C. Mutations in cytoplasmic dynein and its regulators cause malformations of cortical development and neurodegenerative diseases. *Biochem. Soc. Trans.* **41**, 1605–1612 (2013).
- Olenick, M. A. & Holzbaur, E. L. F. Dynein activators and adaptors at a glance. *J. Cell Sci.* **132**, jcs227132 (2019).
- Reck-Peterson, S. L. et al. Single-molecule analysis of dynein processivity and stepping behavior. *Cell* **126**, 335–348 (2006).
- Troktar, M., Mücke, N. & Surrey, T. Reconstitution of the human cytoplasmic dynein complex. *Proc. Natl Acad. Sci. USA* **109**, 20895–20900 (2012).
- Moore, J. K., Stuchell-Brereton, M. D. & Cooper, J. A. Function of dynein in budding yeast: mitotic spindle positioning in a polarized cell. *Cell Motil. Cytoskeleton* **66**, 546–555 (2009).
- Zhang, K. et al. Cryo-EM reveals how human cytoplasmic dynein is auto-inhibited and activated. *Cell* **169**, 1303–1314 (2017).
- Torisawa, T. et al. Autoinhibition and cooperative activation mechanisms of cytoplasmic dynein. *Nat. Cell Biol.* **16**, 1118–1124 (2014).
- Geiser, J. R. et al. *Saccharomyces cerevisiae* genes required in the absence of the CIN8-encoded spindle motor act in functionally diverse mitotic pathways. *Mol. Biol. Cell.* **8**, 1035–1050 (1997).
- Xiang, X., Osmani, A. H., Osmani, S. A., Xin, M. & Morris, N. R. *NudF*, a nuclear migration gene in *Aspergillus nidulans*, is similar to the human LIS-1 gene required for neuronal migration. *Mol. Biol. Cell* **6**, 297–310 (1995).
- Liu, Z., Xie, T. & Steward, R. *Lis1*, the *Drosophila* homolog of a human lissencephaly disease gene, is required for germline cell division and oocyte differentiation. *Development* **126**, 4477–4488 (1999).
- Lam, C., Vergnolle, M. A. S., Thorpe, L., Woodman, P. G. & Allan, V. J. Functional interplay between LIS1, NDE1 and NDEL1 in dynein-dependent organelle positioning. *J. Cell Sci.* **123**, 202–212 (2010).
- Splinter, D. et al. BICD2, dynactin, and LIS1 cooperate in regulating dynein recruitment to cellular structures. *Mol. Biol. Cell* **23**, 4226–4241 (2012).
- Lenz, J. H., Schuchardt, I., Straube, A. & Steinberg, G. A dynein loading zone for retrograde endosome motility at microtubule plus-ends. *EMBO J.* **25**, 2275–2286 (2006).
- Moughamian, A. J., Osborn, G. E., Lazarus, J. E., Maday, S. & Holzbaur, E. L. F. Ordered recruitment of dynactin to the microtubule plus-end is required for efficient initiation of retrograde axonal transport. *J. Neurosci.* **33**, 13190–13203 (2013).
- Lee, W.-L., Oberle, J. R. & Cooper, J. A. The role of the lissencephaly protein Pac1 during nuclear migration in budding yeast. *J. Cell Biol.* **160**, 355–364 (2003).
- Tsai, J.-W., Chen, Y., Kriegstein, A. R. & Vallee, R. B. LIS1 RNA interference blocks neural stem cell division, morphogenesis, and motility at multiple stages. *J. Cell Biol.* **170**, 935–945 (2005).
- Tanaka, T. et al. Lis1 and doublecortin function with dynein to mediate coupling of the nucleus to the centrosome in neuronal migration. *J. Cell Biol.* **165**, 709–721 (2004).
- Dix, C. I. et al. Lissencephaly-1 promotes the recruitment of dynein and dynactin to transported mRNAs. *J. Cell Biol.* **202**, 479–494 (2013).
- Reiner, O. et al. Isolation of a Miller-Dieker lissencephaly gene containing G protein beta-subunit-like repeats. *Nature* **364**, 717–721 (1993).
- Kim, M. H. et al. The structure of the N-terminal domain of the product of the lissencephaly gene *Lis1* and its functional implications. *Structure* **12**, 987–998 (2004).
- Tarricone, C. et al. Coupling PAF signaling to dynein regulation: structure of LIS1 in complex with PAF-acetylhydrolase. *Neuron* **44**, 809–821 (2004).
- Toropova, K. et al. Lis1 regulates dynein by sterically blocking its mechanochemical cycle. *eLife* **3**, e03372 (2014).
- Huang, J. J., Roberts, A. J. A., Leschziner, A. E. A. & Reck-Peterson, S. L. S. Lis1 acts as a 'clutch' between the ATPase and microtubule-binding domains of the dynein motor. *Cell* **150**, 975–986 (2012).
- DeSantis, M. E. et al. Lis1 has two opposing modes of regulating cytoplasmic dynein. *Cell* **170**, 1197–1208 (2017).
- Yamada, M. et al. LIS1 and NDEL1 coordinate the plus-end-directed transport of cytoplasmic dynein. *EMBO J.* **27**, 2471–2483 (2008).
- Mckenney, R. J., Vershinin, M., Kunwar, A., Vallee, R. B. & Gross, S. P. LIS1 and NudE induce a persistent dynein force-producing state. *Cell* **141**, 304–314 (2010).
- Baumbach, J. et al. Lissencephaly-1 is a context-dependent regulator of the human dynein complex. *eLife* **6**, e21768 (2017).
- Gutierrez, P. A., Ackermann, B. E., Vershinin, M. & Mckenney, R. J. Differential effects of the dynein-regulatory factor lissencephaly-1 on processive dynein-dynactin motility. *J. Biol. Chem.* **292**, 12245–12255 (2017).
- Redwine, W. B. et al. The human cytoplasmic dynein interactome reveals novel activators of motility. *eLife* **6**, e28257 (2017).
- Hoogenraad, C. C. et al. Mammalian Golgi-associated bicaudal-D2 functions in the dynein-dynactin pathway by interacting with these complexes. *EMBO J.* **20**, 4041–4054 (2001).
- Hoogenraad, C. C. et al. Bicaudal D induces selective dynein-mediated microtubule minus end-directed transport. *EMBO J.* **22**, 6004–6015 (2003).
- Torisawa, T. et al. Functional dissection of LIS1 and NDEL1 towards understanding the molecular mechanisms of cytoplasmic dynein regulation. *J. Biol. Chem.* **286**, 1959–1965 (2011).
- Wang, S. et al. Nudel/NudE and Lis1 promote dynein and dynactin interaction in the context of spindle morphogenesis. *Mol. Biol. Cell* **24**, 3522–3533 (2013).
- Kapitein, L. C. et al. Probing intracellular motor protein activity using an inducible cargo trafficking assay. *Biophys. J.* **99**, 2143–2152 (2010).
- Tai, C.-Y., Dujardin, D. L., Faulkner, N. E. & Vallee, R. B. Role of dynein, dynactin, and CLIP-170 interactions in LIS1 kinetochore function. *J. Cell Biol.* **156**, 959–968 (2002).
- Sasaki, S. et al. A LIS1/NUDEL/cytoplasmic dynein heavy chain complex in the developing and adult nervous system. *Neuron* **28**, 681–696 (2000).
- Schmidt, H. & Carter, A. P. Review: structure and mechanism of the dynein motor ATPase. *Biopolymers* **105**, 557–567 (2016).
- Schmidt, H., Zalyte, R., Urnavicius, L. & Carter, A. P. Structure of human cytoplasmic dynein-2 primed for its power stroke. *Nature* **518**, 435–438 (2015).
- Elshenawy, M. M. et al. Lis1 activates dynein motility by modulating its pairing with dynactin. *Nat. Cell Biol.* <https://doi.org/10.1038/s41556-020-0501-4> (2020).
- Qiu, R., Zhang, J. & Xiang, X. LIS1 regulates cargo-adapter-mediated activation of dynein by overcoming its autoinhibition in vivo. *J. Cell Biol.* **218**, 3630–3646 (2019).
- Marzo, M. G., Griswold, J. M. & Markus, S. M. Pac1/LIS1 stabilizes an uninhibited conformation of dynein to coordinate its localization and activity. *Nat. Cell Biol.* <https://doi.org/10.1038/s41556-020-0492-1> (2020).
- Sheeman, B. et al. Determinants of *S. cerevisiae* dynein localization and activation: implications for the mechanism of spindle positioning. *Curr. Biol.* **13**, 364–372 (2003).
- Egan, M. J., Tan, K. & Reck-Peterson, S. L. Lis1 is an initiation factor for dynein-driven organelle transport. *J. Cell Biol.* **197**, 971–982 (2012).

Publisher's note Springer Nature remains neutral with regard to jurisdictional claims in published maps and institutional affiliations.

© The Author(s), under exclusive licence to Springer Nature Limited 2020

Methods

Cloning, plasmid construction and mutagenesis. The pDyn1 plasmid (the pACEBac1 expression vector containing insect-cell codon-optimized dynein heavy chain (*DYNC1H1*) fused to a His-ZZ-TEV tag on the amino-terminus and a carboxy-terminal SNAPf tag (New England Biolabs)) and the pDyn2 plasmid (the pIDC expression vector with codon optimized *DYNC1I2*, *DYNC1L2*, *DYNLT1*, *DYNLL1* and *DYNLRB1*) were recombined in vitro with a Cre recombinase (New England Biolabs) to generate the pDyn3 plasmid. The presence of all six dynein chains was verified using PCR. pDyn1, pDyn2 and the pFastBac plasmid with codon-optimized human full-length LIS1 (*PAFAH1B1*) fused to an amino-terminal His-ZZ-TEV tag and pFastBac containing human dynein monomer (amino acids 1320–4646 of *DYNC1H1*) were gifts from A. Carter (LMB-MRC). BicD2 constructs were amplified from a human cDNA library generated from RPE1 cells and the other activating adaptor constructs were obtained as described previously³⁵. Activating adaptors were fused to a ZZ-TEV-HaloTag (Promega) on the amino-terminus and inserted into a pET28a expression vector. All additional tags were added using Gibson assembly and all mutations and truncations were performed using site-directed mutagenesis (Agilent). For rapalog-induced motility in cells, HaloTag-BicD2-S was cloned into the pcDNA5 backbone with a carboxy-terminal V5 epitope tag fused to FRB. The peroxisome tag PEX3 was cloned into pcDNA5 with a carboxy-terminal mEmerald fluorescent protein and FKBP.

Protein expression and purification. Human full-length dynein, human dynein monomer and human LIS1 constructs were expressed in Sf9 cells as described previously^{3,33}. In brief, the pDyn3 plasmid containing the human dynein genes or the pFastBac plasmid containing full-length LIS1 or dynein monomer was transformed into DH10EmBacY chemically competent cells with heat shock at 42 °C for 15 s followed by incubation at 37 °C for 5 h in SOC medium (Thermo Fisher Scientific). The cells were then plated onto LB agar plates containing kanamycin (50 µg ml⁻¹), gentamicin (7 µg ml⁻¹), tetracycline (10 µg ml⁻¹), BluoGal (100 µg ml⁻¹) and isopropyl-β-D-thiogalactoside (IPTG; 40 µg ml⁻¹) and positive clones were identified by a blue/white colour screen after 48 h. For full-length human dynein constructs, white colonies were additionally tested for the presence of all six dynein genes using PCR. These colonies were then grown overnight in LB medium containing kanamycin (50 µg ml⁻¹), gentamicin (7 µg ml⁻¹) and tetracycline (10 µg ml⁻¹) at 37 °C. Bacmid DNA was extracted from overnight cultures using an isopropanol precipitation method as described previously¹². We transfected 2 ml of Sf9 cells at 0.5 × 10⁶ cells per ml with 2 µg of fresh bacmid DNA and FuGene HD transfection reagent (Promega) at a ratio of 3:1 transfection reagent to DNA according to the manufacturer's instructions. After 3 d, the supernatant containing the V0 virus was collected by centrifugation at 200g for 5 min at 4 °C. To generate V1, 1 ml of the V0 virus was used to transfect 50 ml of Sf9 cells at 1 × 10⁶ cells per ml. After 3 d, the supernatant containing the V1 virus was collected by centrifugation at 200g for 5 min at 4 °C and stored in the dark at 4 °C until use. For protein expression, 4 ml of the V1 virus was used to transfect 400 ml of Sf9 cells at 1 × 10⁶ cells per ml. After 3 d, the cells were collected by centrifugation at 3,000g for 10 min at 4 °C. The pellet was resuspended in 10 ml of ice-cold PBS and pelleted again. The pellet was flash-frozen in liquid nitrogen and stored at -80 °C.

Protein purification steps were performed at 4 °C unless otherwise indicated. Full-length dynein and dynein monomer were purified from frozen Sf9 pellets transfected with the V1 virus as described previously³. Frozen cell pellets from a 400 ml culture were resuspended in 40 ml of dynein-lysis buffer (50 mM HEPES pH 7.4, 100 mM sodium chloride, 1 mM dithiothreitol (DTT), 0.1 mM Mg-ATP, 0.5 mM Pefabloc and 10% (v/v) glycerol) supplemented with 1 cOmplete EDTA-free protease inhibitor cocktail tablet (Roche) per 50 ml and lysed using a Dounce homogenizer (10 strokes with a loose plunger and 15 strokes with a tight plunger). The lysate was clarified by centrifuging at 183,960g for 88 min in a Type 70 Ti rotor (Beckman). The clarified supernatant was incubated with 4 ml of IgG Sepharose 6 Fast Flow beads (GE Healthcare Life Sciences) for 3–4 h on a roller. The beads were transferred to a gravity flow column, washed with 200 ml of dynein-lysis buffer and 300 ml of TEV buffer (50 mM Tris-HCl pH 8.0, 250 mM potassium acetate, 2 mM magnesium acetate, 1 mM EGTA, 1 mM DTT, 0.1 mM Mg-ATP and 10% (v/v) glycerol). For fluorescent labelling of carboxy-terminal SNAPf tag, dynein-coated beads were labelled with 5 µM SNAP-Cell-TMR (New England Biolabs) in the column for 10 min at room temperature and unbound dye was removed with a 300 ml wash with TEV buffer at 4 °C. The beads were then resuspended and incubated in 15 ml of TEV buffer supplemented with 0.5 mM Pefabloc and 0.2 mg ml⁻¹ TEV protease (purified in the Reck-Peterson laboratory) overnight on a roller. The supernatant containing cleaved proteins was concentrated using a 100 kDa molecular weight cut-off (MWCO) concentrator (EMD Millipore) to 500 µl and purified using size-exclusion chromatography on a TSKgel G4000SWXL column (TOSOH Bioscience) with GF150 buffer (25 mM HEPES pH 7.4, 150 mM KCl, 1 mM MgCl₂, 5 mM DTT and 0.1 mM Mg-ATP) at 1 ml min⁻¹. The peak fractions were collected, buffer-exchanged into a GF150 buffer supplemented with 10% glycerol, concentrated to 0.1–0.5 mg ml⁻¹ using a 100 kDa MWCO concentrator (EMD Millipore) and flash-frozen in liquid nitrogen.

LIS1 constructs were purified from frozen cell pellets from a 400 ml culture. Lysis and clarification steps were similar to that described for full-length dynein purification except we used LIS1-lysis buffer (30 mM HEPES pH 7.4, 50 mM potassium acetate, 2 mM magnesium acetate, 1 mM EGTA, 300 mM potassium chloride, 1 mM DTT, 0.5 mM Pefabloc and 10% (v/v) glycerol) supplemented with 1 cOmplete EDTA-free protease inhibitor cocktail tablet (Roche) per 50 ml. The clarified supernatant was incubated with 0.5 ml of IgG Sepharose 6 Fast Flow beads (GE Healthcare Life Sciences) for 2–3 h on a roller. The beads were transferred to a gravity flow column, washed with 20 ml of LIS1-lysis buffer, 100 ml of modified TEV buffer (10 mM Tris-HCl pH 8.0, 2 mM magnesium acetate, 150 mM potassium acetate, 1 mM EGTA, 1 mM DTT and 10% (v/v) glycerol) supplemented with 100 mM potassium acetate, and 50 ml of modified TEV buffer. For fluorescent labelling of LIS1 constructs with amino-terminal HaloTags, LIS1-coated beads were labelled with 200 µM Halo-TMR (Promega) for 2.5 h at 4 °C on a roller and the unbound dye was removed with a 200 ml wash with modified TEV buffer supplemented with 250 mM potassium acetate. LIS1 was cleaved from IgG beads by incubation with 0.2 mg ml⁻¹ TEV protease overnight on a roller. The cleaved LIS1 was filtered by centrifuging using an Ultrafree-MC VV filter (EMD Millipore) in a tabletop centrifuge and flash-frozen in liquid nitrogen.

Dynactin was purified from stable HEK293T cell lines expressing p62-Halo-3xFlag as described previously³⁵. In brief, frozen pellets collected from 160 × 15 cm plates were resuspended in 80 ml of dynactin-lysis buffer (30 mM HEPES pH 7.4, 50 mM potassium acetate, 2 mM magnesium acetate, 1 mM EGTA, 1 mM DTT and 10% (v/v) glycerol) supplemented with 0.5 mM Mg-ATP, 0.2% Triton X-100 and 1 cOmplete EDTA-free protease inhibitor cocktail tablet (Roche) per 50 ml and rotated slowly for 15 min. The lysate was clarified by centrifuging at 66,000g for 30 min in a Type 70 Ti rotor (Beckman). The clarified supernatant was incubated with 1.5 ml of anti-Flag M2 affinity gel (Sigma-Aldrich) overnight on a roller. The beads were transferred to a gravity-flow column, washed with 50 ml of wash buffer (dynactin-lysis buffer supplemented with 0.1 mM Mg-ATP, 0.5 mM Pefabloc and 0.02% Triton X-100), 100 ml of wash buffer supplemented with 250 mM potassium acetate, and again with 100 ml of wash buffer. For fluorescent labelling of the HaloTag, dynactin-coated beads were labelled with 5 µM Halo-JF646 (Janelia) in the column for 10 min at room temperature and the unbound dye was washed with 100 ml of wash buffer at 4 °C. Dynactin was eluted from beads with 1 ml of elution buffer (wash buffer with 2 mg ml⁻¹ of 3xFlag peptide). The eluate was collected, filtered by centrifuging with Ultrafree-MC VV filter (EMD Millipore) in a tabletop centrifuge and diluted to 2 ml in buffer A (50 mM Tris-HCl pH 8.0, 2 mM magnesium acetate, 1 mM EGTA and 1 mM DTT) and injected into a MonoQ 5/50 GL column (GE Healthcare and Life Sciences) at 1 ml min⁻¹. The column was prewashed with 10 column volumes (CV) of buffer A, 10 CV of buffer B (50 mM Tris-HCl pH 8.0, 2 mM magnesium acetate, 1 mM EGTA, 1 mM DTT and 1 M potassium acetate) and again with 10 CV of buffer A at 1 ml min⁻¹. To elute, a linear gradient was run over 26 CV from 35–100% buffer B. Pure dynactin complex eluted from ~75–80% buffer B. Peak fractions containing pure dynactin complex were pooled, buffer-exchanged into a GF150 buffer supplemented with 10% glycerol, concentrated to 0.02–0.1 mg ml⁻¹ using a 100 kDa MWCO concentrator (EMD Millipore) and flash-frozen in liquid nitrogen.

Activating adaptors containing amino-terminal HaloTags were expressed in BL-21[DE3] cells (New England Biolabs) at an optical density at 600 nm of 0.4–0.6 with 0.1 mM IPTG for 16 h at 18 °C. Frozen cell pellets from a 2 l culture were resuspended in 60 ml of activating-adaptor-lysis buffer (30 mM HEPES pH 7.4, 50 mM potassium acetate, 2 mM magnesium acetate, 1 mM EGTA, 1 mM DTT and 0.5 mM Pefabloc, 10% (v/v) glycerol) supplemented with 1 cOmplete EDTA-free protease inhibitor cocktail tablet (Roche) per 50 ml and 1 mg ml⁻¹ lysozyme. The resuspension was incubated on ice for 30 min and lysed by sonication. The lysate was clarified by centrifuging at 66,000g for 30 min in Type 70 Ti rotor (Beckman). The clarified supernatant was incubated with 2 ml of IgG Sepharose 6 Fast Flow beads (GE Healthcare Life Sciences) for 2 h on a roller. The beads were transferred into a gravity-flow column, washed with 100 ml of activating-adaptor-lysis buffer supplemented with 150 mM potassium acetate and 50 ml of cleavage buffer (50 mM Tris-HCl pH 8.0, 150 mM potassium acetate, 2 mM magnesium acetate, 1 mM EGTA, 1 mM DTT, 0.5 mM Pefabloc and 10% (v/v) glycerol). The beads were then resuspended and incubated in 15 ml of cleavage buffer supplemented with 0.2 mg ml⁻¹ TEV protease overnight on a roller. The supernatant containing cleaved proteins was concentrated using a 50 kDa MWCO concentrator (EMD Millipore) to 1 ml, filtered by centrifuging with Ultrafree-MC VV filter (EMD Millipore) in a tabletop centrifuge, diluted to 2 ml in buffer A (30 mM HEPES pH 7.4, 50 mM potassium acetate, 2 mM magnesium acetate, 1 mM EGTA, 10% (v/v) glycerol and 1 mM DTT) and injected into a MonoQ 5/50 GL column (GE Healthcare and Life Sciences) at 1 ml min⁻¹. The column was prewashed with 10 CV of buffer A, 10 CV of buffer B (30 mM HEPES pH 7.4, 1 M potassium acetate, 2 mM magnesium acetate, 1 mM EGTA, 10% (v/v) glycerol and 1 mM DTT) and again with 10 CV of buffer A at 1 ml min⁻¹. To elute, a linear gradient was run over 26 CV from 0–100% buffer B. The peak fractions containing Halo-tagged activating adaptors were collected and concentrated to using a 50 kDa MWCO concentrator (EMD Millipore) to 0.2 ml. For fluorescent labelling of the HaloTag, the concentrated peak fractions were incubated with 5 µM Halo-Alexa488 (Promega) for 10 min at room temperature. Unbound dye was removed using a PD-10 desalting column (GE Healthcare and Life Sciences) according to the manufacturer's instructions.

The labelled activating adaptor sample was concentrated using a 50 kDa MWCO concentrator (EMD Millipore) to 0.2 ml, diluted to 0.5 ml in GF150 buffer and further purified using size-exclusion chromatography on a Superose 6 Increase 10/300 GL column (GE Healthcare and Life Sciences) with GF150 buffer at 0.5 ml min⁻¹. The peak fractions were collected, buffer-exchanged into a GF150 buffer supplemented with 10% glycerol, concentrated to 0.2–1 mg ml⁻¹ using a 50 kDa MWCO concentrator (EMD Millipore) and flash-frozen in liquid nitrogen.

For the two-colour dynein experiments shown in Fig. 3, the labelling efficiency of TMR-dynein was 94% for one biological replicate and 87% for the other, and the labelling efficiency of Alexa647-dynein was 96% for one biological replicate and 100% for the other. For the two-colour experiment shown in Fig. 4, the labelling efficiency of Alexa647-dynein and TMR-LIS1 was 100% and 93%, respectively. For the two-colour experiment shown in Extended Data Fig. 4, the labelling efficiency of Alexa647-dynein and TMR-LIS1-5A was 100% and 87%, respectively. For the two-colour dynein experiments shown in Fig. 5, the labelling efficiency of both TMR-dynein and Alexa647-dynein was 100%.

Single-molecule TIRF microscopy. Single-molecule imaging was performed using an inverted microscope (Nikon, Ti-E Eclipse) equipped with a ×100/1.49 NA oil-immersion objective (Nikon, Plano Apo) and a ProScan linear motor stage controller (Prior). The microscope was equipped with a LU-NV laser launch (Nikon), with 405 nm, 488 nm, 532 nm, 561 nm and 640 nm laser lines. The excitation and emission paths were filtered using appropriate single bandpass filter cubes (Chroma). For two-colour colocalization imaging, the emission signals were further filtered and split using W-view Gemini image splitting optics (Hamamatsu). The emitted signals were detected using an electron multiplying CCD camera (Andor Technology, iXon Ultra 897). Illumination and image acquisition was controlled by NIS Elements Advanced Research software (Nikon).

Single-molecule motility and microtubule binding assays were performed in flow chambers assembled as described previously⁵⁰ using the TIRF microscopy setup described above. Either biotin-PEG-functionalized coverslips (Microsurfaces) or No. 1-1/2 coverslips (Corning) sonicated in 100% ethanol for 10 min were used for the flow-chamber assembly. Taxol-stabilized microtubules with ~10% biotin-tubulin and ~10% fluorescent tubulin (labelled with Alexa405, Alexa488 or Alexa647) were prepared as described previously⁵¹. Flow chambers were assembled with taxol-stabilized microtubules by incubating sequentially with the following solutions, interspersed with two washes with assay buffer (30 mM HEPES pH 7.4, 2 mM magnesium acetate, 1 mM EGTA, 10% glycerol and 1 mM DTT) supplemented with 20 μM taxol in between: (1) 1 mg ml⁻¹ biotin-BSA in assay buffer (3 min incubation); (2) 0.5 mg ml⁻¹ streptavidin in assay buffer (3 min incubation); and (3) a fresh dilution of taxol-stabilized microtubules in assay buffer (3 min incubation). After flowing in microtubules, the flow chamber was washed twice with assay buffer supplemented with 1 mg ml⁻¹ casein and 20 μM taxol.

To assemble dynein-dynactin-activating adaptor complexes, purified dynein (10–20 nM concentration), dynactin and the activating adaptor were mixed at a molar ratio of 1:2:10 and incubated on ice for 10 min. These dynein-dynactin-activating adaptor complexes were then incubated with LIS1 or modified TEV buffer (to buffer match for experiments without LIS1) for 10 min on ice. Dynactin and the activating adaptors were omitted for the experiments with dynein alone. The mixtures of dynein, dynactin and activating adaptor, or dynein alone, and LIS1 were then flowed into the flow chamber assembled with taxol-stabilized microtubules. The final imaging buffer contained the assay buffer supplemented with 20 μM taxol, 1 mg ml⁻¹ casein, 71.5 mM β-mercaptoethanol, an oxygen scavenger system and 2.5 mM Mg-ATP. The final concentration of dynein in the flow chamber was 0.5–1 nM for experiments with dynein-dynactin-activating adaptor complexes and 0.3–0.5 nM for dynein alone experiments. The final concentration of LIS1 was between 12 nM–300 nM (as indicated in the main text) for experiments with unlabelled LIS1, and 50 nM for experiments with TMR-labelled LIS1. For standard motility experiments, our final imaging buffer contained 30 mM potassium acetate and 7.5 mM KCl. For the experiments shown in Figs. 2 and 3, the increased-ionic-strength buffer contained 60 mM potassium acetate and 7.5 mM KCl. We selected this salt condition because it resulted in severely compromised the motility of dynein-dynactin-Hook3 complexes.

For single-molecule motility assays, microtubules were imaged first by taking a single-frame snapshot. Dynein and/or the activating adaptor labelled with fluorophores (TMR, Alexa647 or Alexa488) was imaged every 300 ms for 3 min. At the end, microtubules were imaged again by taking a snapshot to assess stage drift. Videos showing substantial drift were not analysed. Each sample was imaged for no longer than 15 min. For single-molecule microtubule binding assays, the final imaging mixture containing dynein was incubated for an additional 5 min in the flow chamber at room temperature before imaging. After 5 min incubation, microtubules were imaged first by taking a single-frame snapshot. Dynein and/or activating adaptors labelled with fluorophores (TMR, Alexa647 or Alexa488) were imaged by taking a single-frame snapshot. Each sample was imaged at four different fields of view and there were between five and ten microtubules in each field of view. To compare the effect of LIS1 on microtubule binding, the samples with and without LIS1 were imaged in two separate flow chambers made on the same coverslip on the same day with the same stock of polymerized tubulin as described previously⁵¹.

Microtubule gliding assays. For microtubule gliding assays, 30 nM TMR-dynein in GF150 was flowed into the chamber and non-specifically bound to the coverslip. After 3 min, the chamber was washed twice with BRB80 buffer (80 mM PIPES pH 6.8, 2 mM MgCl₂, 1 mM EGTA) supplemented with 1 mg ml⁻¹ casein, and then with the same buffer containing 5 mg ml⁻¹ casein for 3 min. Next, the chamber was washed twice with BRB80 buffer with casein. Finally, GMPCPP-stabilized microtubules (polymerized with 10% Alexa488-tubulin) were added in the presence or absence of LIS1. The final imaging buffer contained BRB80 buffer supplemented with 20 μM taxol, 1 mg ml⁻¹ casein, 71.5 mM β-mercaptoethanol, an oxygen scavenger system and 2.5 mM Mg-ATP. Microtubules were incubated for 3 min, and then two fields of view were imaged at 1 s per frame for 3 min.

Single-molecule motility assay analysis. Kymographs were generated from motility videos and dynein velocity was calculated from kymographs using ImageJ macros as described previously⁵¹. Only runs that were longer than four frames (1.2 s) were included in the analysis. Bright aggregates, which were less than 5% of the population, were excluded from the analysis. Stationary and diffusive events were grouped as non-processive events when calculating the percentage of events that were processive. For two-colour colocalization analysis, kymographs from each channel were generated and merged in ImageJ and the number of colocalized runs was determined manually. For two-colour colocalization and percentage processive analysis, data from all replicates were pooled and χ^2 tests were performed. Data plotting and statistical analyses were performed in Prism 8 (GraphPad).

Single-molecule microtubule-binding assay analysis. Intensity profiles of dynein or activating adaptor spots from a single-frame snapshot were generated over a line (width, 5 px) drawn perpendicular to the long axis of microtubules in ImageJ. Intensity peaks at least twofold higher than the neighbouring background intensity were counted as dynein or activating-adaptor spots bound to microtubules. Bright aggregates that were fivefold brighter than the neighbouring intensity peaks were not counted. The average binding density was calculated as the total number of dynein or activating adaptor spots divided by the total microtubule length in each snapshot. Normalized binding density was calculated by dividing by the average binding density of dynein or activating adaptor without LIS1 collected on the same coverslip (see above). Data plotting and statistical analyses were performed in Prism 7 (GraphPad).

Microtubule gliding assay analysis. Kymographs were generated by tracing the path of individual microtubules and velocity was calculated from kymographs using ImageJ macros as described previously⁵¹. Data plotting and statistical analyses were performed in Prism 8 (GraphPad).

Protein-binding assays. To assess dynein-dynactin complex formation, BicD2-S was first coupled to 15 μl of Magne HaloTag Beads (Promega) in 2 ml Protein Lo Bind Tubes (Eppendorf) using the following protocol. Beads were washed twice with 1 ml of GF150 without ATP supplemented with 10% glycerol and 0.1% NP-40. BicD2-S was diluted in this buffer to 75 nM. We added 25 μl of diluted BicD2-S to the beads and gently shook for 1 h. We then analysed 20 μl of supernatant using SDS-PAGE to confirm complete depletion of BicD2-S. The BicD2-S-conjugated beads were washed once with 1 ml GF150 with 10% glycerol and 0.1% NP-40 and once with 1 ml of binding buffer (30 mM HEPES pH 7.4, 2 mM magnesium acetate, 1 mM EGTA, 10% glycerol, 1 mM DTT, 1 mg ml⁻¹ casein, 0.1% NP-40 and 1 mM ADP) supplemented with 15.7 mM KCl and 8.3 mM potassium acetate. We diluted 10 nM dynein, 10 nM dynactin and 150 nM LIS1 in binding buffer, which resulted in 15.7 mM KCl and 8.3 mM potassium acetate. We used a molar ratio of dynein, dynactin and BicD2-S of 1:1:7.5 because, at this ratio, dynein bound to BicD2-S minimally in the absence of LIS1. This provided us a large dynamic range to observe the LIS1-induced increase in binding. For experiments lacking dynactin or LIS1, the protein dilutions were supplemented with the equivalent mass of BSA in the equivalent amount of their purification buffers. We added 25 μl of the dynein, dynactin and LIS1 mixture to the beads prebound with BicD2-S and gently agitated for 45 min. After incubation, 20 μl of the supernatant was removed, and 6.67 μl of NuPAGE LDS sample buffer (4×) and 1.33 μl of β-mercaptoethanol was added to each. The samples were boiled for 5 min before running on a 4–12% NuPAGE Bis-Tris gel at 4°C. Depletion was determined using densitometry in ImageJ.

LIS1-binding curves were determined as described above with minor variations. We used 25 μl of Magne HaloTag Beads, and washed twice with 1 ml modified TEV buffer. Lis 1 (0 nM, 30 nM, 60 nM, 90 nM, 120 nM, 300 nM and 600 nM) was bound to beads for 1 h at ambient temperature. Beads were then washed with 1 ml of modified TEV buffer and 1 ml of binding buffer supplemented with 30 mM KCl and 6 mM potassium acetate. We diluted 10 nM dynein in binding buffer supplemented with salt to 30 mM KCl and 6 mM potassium acetate. Binding and determination of depletion were performed as described above. Binding curves were fit in Prism 8 (GraphPad) with a nonlinear regression for one-site binding with Bmax set to 1.

Cryo-EM sample preparation. A final concentration of 3.5 μM dynein monomer and 3.5 μM HaloTag-LIS1 were incubated in assay buffer supplemented with DTT, NP-40 and ATP-VO₄ for 10–20 min before grids were prepared. Proteins

were diluted and mixed such that the final salt and additive concentrations were 52.5 mM KCl, 20 mM potassium acetate, 4.8% glycerol, 5 mM DTT, 0.005% NP-40 and 2.5 mM ATPV₀. Sample (4 µl) was applied to UltraAuFoil R 1.2/1.3 300 mesh grids (Electron Microscopy Sciences) that were glow-discharged with 20 mA negative current for 30 s. Grids were plunge-frozen in a Vitrobot Mark IV robot (FEI), maintained at 100% humidity and 4 °C.

Cryo-EM data collection and image analysis. Data were collected using a Talos Arctica transmission electron microscope (FEI) operating at 200 keV with a K2 Summit direct electron detector (Gatan). Dose-fractionated videos were collected in counting mode, with a final calibrated pixel size of 1.16 Å px⁻¹, a dose rate of ~6 e⁻ px⁻¹ s⁻¹ and a total dose of ~60 e⁻ Å⁻². Leginon⁵² was used for automated data collection and videos were processed on-the-fly using Appion⁵³. Video alignment was performed with MotionCor2 defocus estimations were performed with CTFIND4 (ref. ⁵⁴), and particles were picked using DoG Picker⁵⁵; 403,439 particles were extracted from 2,422 aligned, dose weighted micrographs in Relion-3 (ref. ⁵⁶) with a box size of 288 × 288 px and binned by 2 for a final pixel size of 2.32 Å px⁻¹. The extracted particles were imported into cryoSPARC 2.4.2 for all subsequent analysis⁵⁷. To generate the 2D-class averages shown in Fig. 2, two rounds of 2D classification were performed. In the first round, 2D classes containing clear density corresponding to the dynein ATPase ring and LIS1 (comprising 71,436 particles) were selected. In the second round, three classes, containing 22,621 total particles were selected for presentation in Fig. 2 (7,712 particles in the class on the left, 8,943 particles in the class in the middle and 6,506 particles in the class on the right).

To generate a model of human dynein bound to LIS1, we aligned human dynein-2 bound to ATP-vanadate (PDB, 4RH7)⁴⁴ with yeast dynein (AAA3-Walker B) in ATP-vanadate and LIS1 (PDB, 5VLJ)³⁰ using the part of the sequence that encompasses the two LIS1-binding sites in yeast dynein, from AAA3 until after the binding site for the second LIS1 in the stalk. We then deleted the dynein chain of PDB 5VLJ and combined the remaining two copies of LIS1 with PDB 4RH7. To highlight the densities corresponding to LIS1, we also generated 2D projections of human dynein-2 alone (PDB, 4RH7) in the same orientations as our experimental data.

SEC-MALS. Size-exclusion chromatography with multiangle light scattering (SEC-MALS) experiments were performed using an ÅKTAMicro chromatography system connected to a Superdex 200 Increase 3.2/300 size-exclusion chromatography column (GE Healthcare and Life Sciences) coupled in-line to a DAWN HELEOS II multiangle light-scattering detector (Wyatt Technology) and an Optilab T-rEX refractive-index detector (Wyatt Technology). SEC-MALS was performed in 25 mM HEPES pH 7.4, 30 mM KCl, 6 mM potassium acetate, 1 mM MgCl₂, 5 mM DTT and 0.1 mM Mg-ATP flowed at 0.1 ml min⁻¹. A 50 µl sample of 4 µM dynein monomer and/or 2 M LIS1 dimer or 4 µM LIS1ΔN was incubated on ice for 10 min before injection. Molar mass was calculated using ASTRA 6; the protein concentration was derived from the Optilab T-rEX.

Peroxisome recruitment assay. Human U2OS cells were cultured in Dulbecco's modified Eagle's medium containing 10% fetal calf serum and 1% penicillin-streptomycin. One day before transfection, the cells were plated on 35 mM fluorodishes (World Precision Instruments) coated with 100 µg ml⁻¹ poly-D-lysine (Sigma Aldrich) and 4 µg ml⁻¹ mouse laminin (Thermo Fisher Scientific). Cells were transfected with 120 ng PEX3-mEmerald-FKBP and BicD2NS-V5-FRB constructs per well as well as 20 pmol of either ON-TARGETplus Non-targeting siRNA 1 (Dharmacon), ON-TARGETplus PFAH1B1 siRNA J-010330-07-0002 (Dharmacon), ON-TARGETplus PFAH1B1 siRNA J-010330-09-0002 (Dharmacon) or SMARTpool: ON-TARGETplus PFAH1B1 siRNA (Dharmacon) using Lipofectamine 2000 (Thermo Fisher Scientific).

Cells were labelled with Halo-JF549 (Janelia) and imaged after 48 h using a ×100/1.49 NA Apo TIRF objective on a Nikon Ti2 microscope with a Yokogawa-X1 spinning-disk confocal system, MLC400B laser engine (Agilent), Prime 95B back-thinned sCMOS camera (Teledyne Photometrics), piezo Z-stage (Mad City Labs) and stage-top environmental chamber (Tokai Hit). Cells were screened for the presence of JF549 signal with the 560 nm laser line and then mEmerald was imaged at 2 frames per second, 100 ms exposure with the 488 nm laser line. Dimerization of FKBP-FRB was induced using 1 µM rapalog (Takara Bio). Images were analysed in ImageJ. Kymographs were generated from >5 peroxisomes that moved directionally for >3 frames in each cell and velocity was calculated from kymographs using ImageJ macros as described previously³¹. Data plotting and statistical analyses were performed in Prism 8 (GraphPad).

Western-blot analysis and antibodies. Lysates were run on 4–12% polyacrylamide gels (NuPage, Invitrogen) and transferred to polyvinylidene difluoride (Immobilon-P, EMD Millipore) for 1.5 h at 300 mA constant current. Blots were blocked for 10 min with TBS + 5% dry milk (w/v), and were immunoblotted with appropriate antibodies. All antibodies were diluted in TBST + 5% milk (w/v). Primary antibodies were incubated overnight at 4 °C, while secondary antibodies were incubated for 1 h at room temperature. The antibodies used were as follows: mouse anti-LIS1 (sc-374586, Santa Cruz Biotechnology, 1:200 dilution), mouse anti-β-actin (MA5-15739, Invitrogen, 1:2,000 dilution), rabbit anti-V5 (V8137, Sigma-Aldrich, 1:2,000 dilution), goat anti-rabbit HRP (7076, Cell Signaling

Technology, 1:5,000 dilution) and horse anti-mouse HRP (7074, Cell Signaling Technology, 1:5,000 dilution). Western blots were visualized using Supersignal West Pico or Femto Chemiluminescent reagents (Thermo Fisher Scientific) and a VersaDoc imaging system (Bio-Rad Laboratories). Image intensity histograms were adjusted and images were converted to 8-bit using ImageJ before being imported into Adobe Illustrator to generate the figures.

Statistics and reproducibility. Live-cell experiments were performed with two independent cell transfections. At least three individual experiments were performed using two independent purifications of dynein for biochemistry and single-molecule results, with the exception of the SEC-MALS experiments that used a single purification. Each experiment was repeated independently with similar results. The *n* values for each experiment are defined in the figure legends along with a description of the statistical tests performed.

Reporting Summary. Further information on research design is available in the Nature Research Reporting Summary linked to this article.

Data availability

No large datasets were generated during this study. Source data for Figs. 1–5 and Extended Data Figs. 1–4 are available with the paper. We encourage anyone who wishes to build on these studies or replicate them to contact the corresponding authors and we will share all plasmids used to generate the proteins used in these studies.

References

- Case, R. B., Pierce, D. W., Hom-Booher, N., Hart, C. L. & Vale, R. D. The directional preference of kinesin motors is specified by an element outside of the motor catalytic domain. *Cell* **90**, 959–966 (1997).
- Roberts, A. J., Goodman, B. S. & Reck-Peterson, S. L. Reconstitution of dynein transport to the microtubule plus end by kinesin. *eLife* **3**, e02641 (2014).
- Scheres, S. H. W. RELION: implementation of a Bayesian approach to cryo-EM structure determination. *J. Struct. Biol.* **180**, 519–530 (2012).
- Lander, G. C. et al. Appion: an integrated, database-driven pipeline to facilitate EM image processing. *J. Struct. Biol.* **166**, 95–102 (2009).
- Zheng, S. Q. et al. MotionCor2: anisotropic correction of beam-induced motion for improved cryo-electron microscopy. *Nat. Methods* **14**, 331–332 (2017).
- Voss, N. R., Yoshioka, C. K., Radermacher, M., Potter, C. S. & Carragher, B. DoG Picker and TiltPicker: software tools to facilitate particle selection in single particle electron microscopy. *J. Struct. Biol.* **166**, 205–213 (2009).
- Zivanov, J. et al. New tools for automated high-resolution cryo-EM structure determination in RELION-3. *eLife* **7**, e42166 (2018).
- Punjani, A., Rubinstein, J. L., Fleet, D. J. & Brubaker, M. A. cryoSPARC: algorithms for rapid unsupervised cryo-EM structure determination. *Nat. Methods* **14**, 290–296 (2017).

Acknowledgements

We thank J. Christensen, E. Karasmanis, A. Kendrick, A. Roberts and J. Sologianis for comments on the manuscript and discussions; staff at the Nikon Imaging Center at UC San Diego, where we collected data and received help with image analysis; staff at the UC San Diego cryo-EM facility, where cryo-EM data were collected; and staff at the Physics Computing Facility for IT support. S.L.R.-P. is supported by HHMI and NIH R01GM121772. Funding to S.L.R.-P. from the HHMI/Simons Faculty Scholars Program and R01GM107214 funded earlier parts of this research. A.E.L. is supported by R01GM107214; Z.M.H. by NSF graduate research fellowship DGE1144152; J.P.G. by the Molecular Biophysics Training Grant, NIH Grant T32 GM008326; R.W.B. is a Damon Runyon Fellow supported by the Damon Runyon Cancer Research Foundation DRG-#2285-17; and M.E.D. by NIH K99GM127757 and previously by a Jane Coffin Childs Memorial Fund Postdoctoral Fellowship 61-1552-T.

Author contributions

Z.M.H., J.P.G., M.E.D., A.E.L. and S.L.R.-P. designed the experiments. Z.M.H., J.P.G., M.E.D. and R.W.B. performed the experiments. Z.M.H., J.P.G., M.E.D., A.E.L. and S.L.R.-P. wrote the manuscript. All of the authors interpreted the data and reviewed and edited the manuscript.

Competing interests

The authors declare no competing interests.

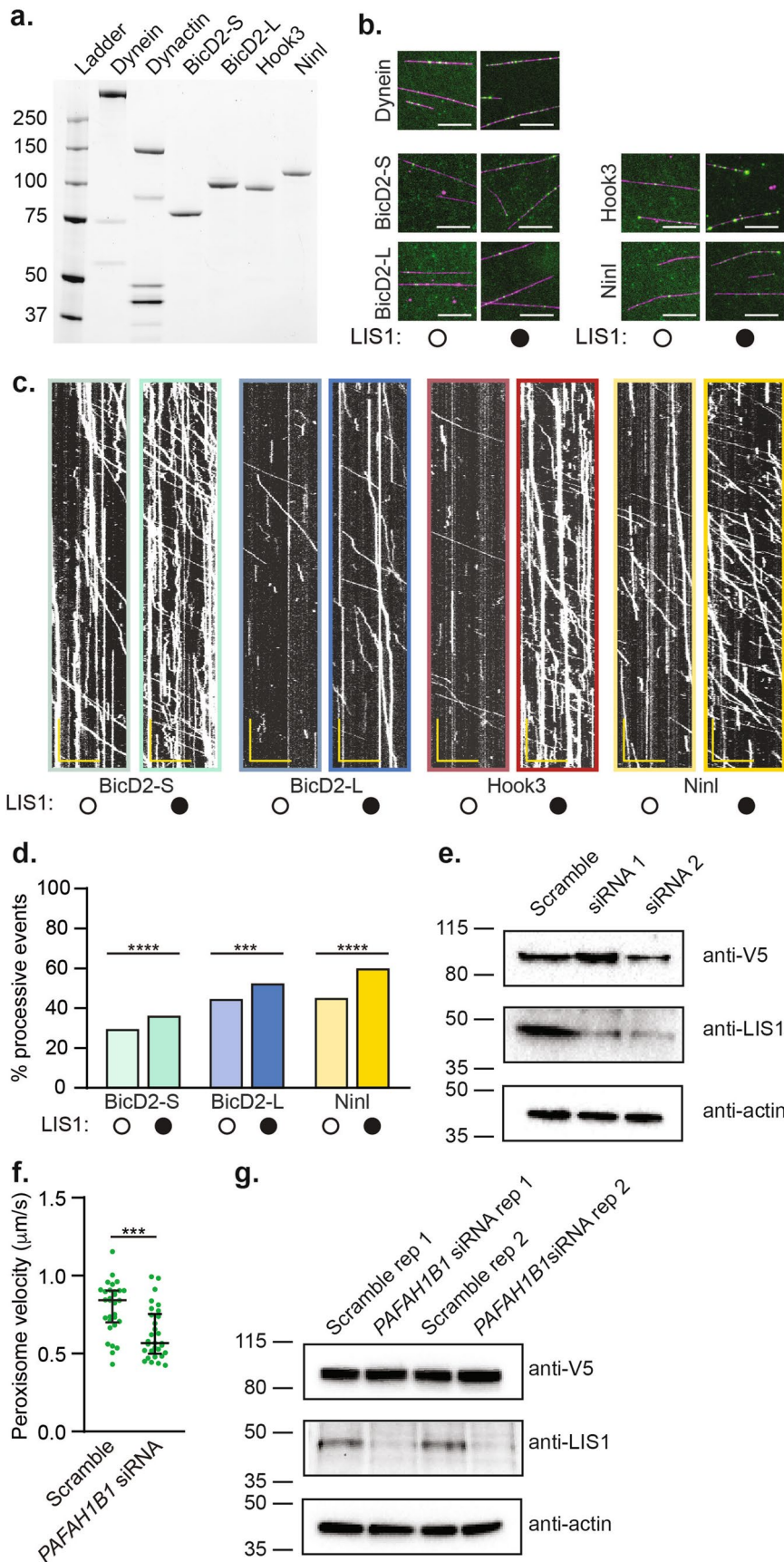
Additional information

Extended data is available for this paper at <https://doi.org/10.1038/s41556-020-0506-z>.

Supplementary information is available for this paper at <https://doi.org/10.1038/s41556-020-0506-z>.

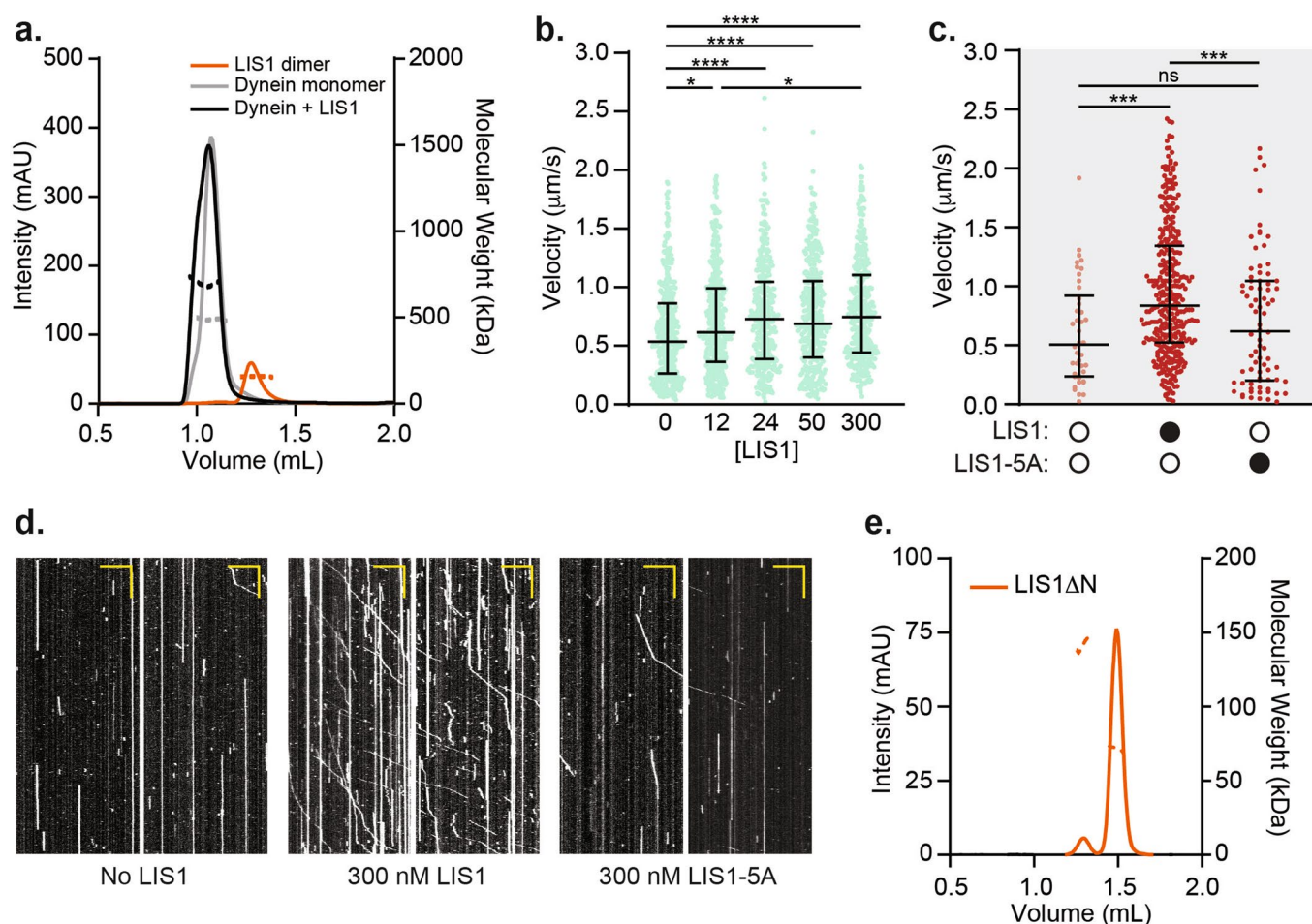
Correspondence and requests for materials should be addressed to M.E.D. or S.L.R.-P.

Reprints and permissions information is available at www.nature.com/reprints.

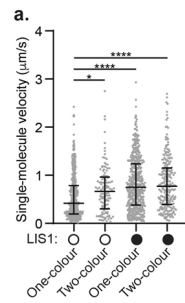


Extended Data Fig. 1 | See next page for caption.

Extended Data Fig. 1 | Effect of Lis1 on the motility and microtubule binding of activated dynein complexes. **a**, SDS-PAGE gel stained with Sypro Red of human dynein, dynactin and the activating adaptors BicD2-S (aa 25-398), BicD2-L (aa 1-598), Hook3 (aa 1-552), and Ninl (aa 1-702) used in this study. The dynein heavy chain was tagged with the SNAP tag, the dynactin subunit p62 with the HaloTag, and each activating adaptor with the HaloTag. The dynein light chains are too small to be seen on this low percentage gel. SDS-PAGE gels were run after all protein purifications. **b**, Example microscopy images for microtubule binding density data in the absence (white circles) or presence (black circles) of 300 nM Lis1 presented in Fig. 1d, e. Microtubules in magenta and dynein or activating adaptor foci in green. Scale bars are 10 μm . **c**, Example kymographs of dynein–dynactin–activating adaptor complexes in the absence (white circles) or presence (black circles) of 300 nM Lis1. Scale bars are 10 μm (x) and 20 sec (y). **d**, Percent processive runs of dynein–dynactin–activating adaptor complexes in standard motility buffer in the absence (white circles) or presence (black circles) of 300 nM Lis1. Statistical analysis was performed on data pooled from all replicates with χ^2 test. **e**, Immunoblots of cell lysates from human U2OS cells co-transfected with PEX3-mEmerald-FKBP and BicD2-S-V5-FRB constructs, as well as either scramble siRNA or Lis1 siRNA 1 or 2. Blots were performed for each biorep with similar results. **f**, Peroxisome velocity in human U2OS cells with scrambled or Lis1 siRNA pool knockdown. The median and interquartile range are shown. At least 7 peroxisome motility events were measured per cell. **g**, Immunoblots of cell lysates from human U2OS cells co-transfected with PEX3-mEmerald-FKBP and BicD2-S-V5-FRB constructs and scramble or Lis1 siRNA pool. Two bio-replicates (1 and 2) are shown. An anti-V5 antibody detects BicD2-S-V5-FRB, an anti-Lis1 antibody assesses the efficiency of Lis1 knockdown, and an anti-actin antibody serves as a loading control for immunoblots shown in e and g. Statistical data and unprocessed gel and blot images are available as source data for Extended Data Fig. 1.

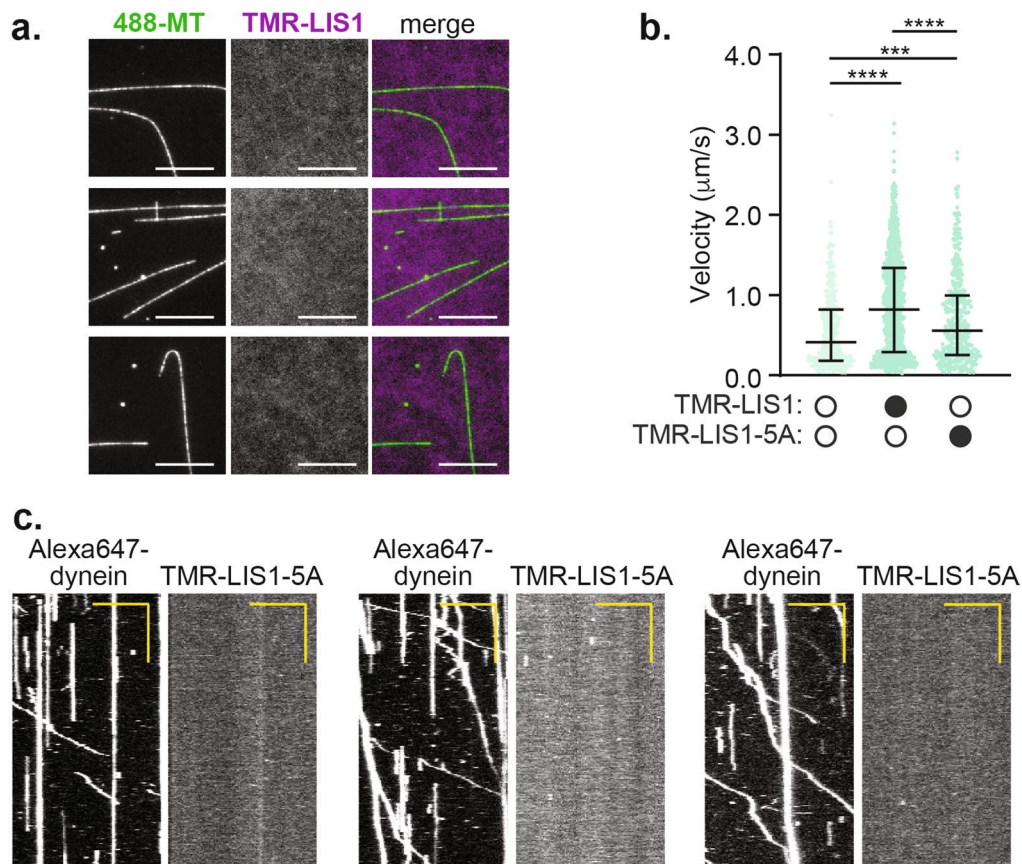


Extended Data Fig. 2 | Characterization of the dynein binding interface and dimerization domain of Lis1. **a**, Example SEC-MALS traces with Lis1 dimer (orange), dynein monomer (grey), and dynein monomer with Lis1 dimer (black). The intensity of the UV signal (solid line) and the molecular weight fit (dashed line) are shown. Dimeric Halo-tagged-Lis1 is expected to be 161.4 kDa and monomeric dynein is expected to be 380.4 kDa. In this experiment we observe Halo-tagged-Lis1 to be 157.6 kDa, monomeric dynein to be 489.5 kDa and the Lis1-dynein complex to be 700.1 kDa. The high apparent molecular weight of monomeric dynein may be due to a self-association species that appears as a shoulder in the UV trace. The experiment was repeated in triplicate yielding similar results, giving a stoichiometry of 1.2 ± 0.3 Lis1 dimers per dynein monomer. Based on this data we cannot rule out that some dynein monomers are bound to two Lis1 dimers (which has been reported to occur³⁴), but our data suggest that most dynein monomers bind a single Lis1 dimer, and that Lis1 does not tether two dynein monomers. **b**, Single-molecule velocity of dynein-dynactin-BicD2-5 complexes with increasing concentrations of Lis1. The median and interquartile range are shown. **c**, Single-molecule velocity of dynein-dynactin-Hook3 complexes in the presence of a higher ionic strength buffer in the absence (white circles) or presence (black circles) of 300 nM Lis1 or Lis1-5A. The data in the presence and absence of WT Lis1 was also presented in Fig. 1g. The median and interquartile range are shown. **d**, Example kymographs of dynein-dynactin-Hook3 complexes in a higher ionic strength buffer in the absence or presence of 300 nM Lis1 or Lis1-5A. Scale bars are 10 μm (x) and 20 sec (y). Data is quantified in Extended Data Fig. 2c. **e**, Example SEC-MALS trace of Lis1 ΔN (orange). The intensity of the UV signal (solid line) and the molecular weight fit (dashed line) are shown. Monomeric Halo-tagged-Lis1 ΔN is expected to be 71.5 kDa. In this experiment we observe Halo-tagged-Lis1 ΔN to have a monomer peak at 72.0 kDa and a dimer peak at 141.2 kDa. The experiment was repeated in triplicate yielding similar results. Statistical data is available as source data for Extended Data Fig. 2.



Extended Data Fig. 3 | Quantification of the velocity of one-color and two-color activated dynein complexes in the presence or absence of Lis1.

a. Single-molecule velocity of dynein-dynactin-BicD2-5 complexes in the absence (white circles) or presence (black circles) of 300 nM Lis1 with colocalized dynein (two color) or without observed colocalization (one color). The median and interquartile range are shown. Statistical data is available as source data for Extended Data Fig. 3.



Extended Data Fig. 4 | Characterization of Lis1 binding to microtubules and activated dynein complexes. **a**, Example microscopy images for imaging 50 nM TMR-Lis1 (magenta in merge) in the presence of microtubules (green in merge). Lis1 does not colocalize with microtubules. Scale bars are 10 μm . The experiment was repeated in triplicate yielding similar results. **b**, Single-molecule velocity of dynein-dynactin-BicD2-S complexes in the absence (white circles) or presence (black circles) of 50 nM TMR-Lis1 or TMR-Lis1-5A. The median and interquartile range are shown. **c**, Representative kymographs of Alexa647-dynein-dynactin-BicD2-S complexes in the presence of 50 nM TMR-Lis1-5A. Scale bars are 10 μm (x) and 20 sec (y). Statistical data is available as source data for Extended Data Fig. 4.

Reporting Summary

Nature Research wishes to improve the reproducibility of the work that we publish. This form provides structure for consistency and transparency in reporting. For further information on Nature Research policies, see [Authors & Referees](#) and the [Editorial Policy Checklist](#).

Statistics

For all statistical analyses, confirm that the following items are present in the figure legend, table legend, main text, or Methods section.

n/a Confirmed

- The exact sample size (n) for each experimental group/condition, given as a discrete number and unit of measurement
- A statement on whether measurements were taken from distinct samples or whether the same sample was measured repeatedly
- The statistical test(s) used AND whether they are one- or two-sided
Only common tests should be described solely by name; describe more complex techniques in the Methods section.
- A description of all covariates tested
- A description of any assumptions or corrections, such as tests of normality and adjustment for multiple comparisons
- A full description of the statistical parameters including central tendency (e.g. means) or other basic estimates (e.g. regression coefficient) AND variation (e.g. standard deviation) or associated estimates of uncertainty (e.g. confidence intervals)
- For null hypothesis testing, the test statistic (e.g. F , t , r) with confidence intervals, effect sizes, degrees of freedom and P value noted
Give P values as exact values whenever suitable.
- For Bayesian analysis, information on the choice of priors and Markov chain Monte Carlo settings
- For hierarchical and complex designs, identification of the appropriate level for tests and full reporting of outcomes
- Estimates of effect sizes (e.g. Cohen's d , Pearson's r), indicating how they were calculated

Our web collection on [statistics for biologists](#) contains articles on many of the points above.

Software and code

Policy information about [availability of computer code](#)

Data collection

For light microscopy experiments, data was collected with Nikon Elements Software (commercially available). For electron microscopy experiments, data was collected and processed with Leginon, Appion, MotionCor2, CTFIND4, DoG Picker, Relion-3, and cryoSPARC 2.4.2.

Data analysis

For light microscopy experiments, data was analyzed with ImageJ 1.52i with a custom macro written to generate kymographs. Prism7 or Prism8 were used for all statistical analysis of light microscopy data. To generate the theoretical 2D class averages shown in figure 2, we used a custom Spider script that will be made available upon request. For SEC-MALS data molar mass was calculated using ASTRA-6 software.

For manuscripts utilizing custom algorithms or software that are central to the research but not yet described in published literature, software must be made available to editors/reviewers. We strongly encourage code deposition in a community repository (e.g. GitHub). See the Nature Research [guidelines for submitting code & software](#) for further information.

Data

Policy information about [availability of data](#)

All manuscripts must include a [data availability statement](#). This statement should provide the following information, where applicable:

- Accession codes, unique identifiers, or web links for publicly available datasets
- A list of figures that have associated raw data
- A description of any restrictions on data availability

No large datasets were generated or analyzed in this study. All the raw data that went into the analysis of each figure were deposited in a spreadsheet with the manuscript.

Field-specific reporting

Please select the one below that is the best fit for your research. If you are not sure, read the appropriate sections before making your selection.

Life sciences Behavioural & social sciences Ecological, evolutionary & environmental sciences

For a reference copy of the document with all sections, see [nature.com/documents/nr-reporting-summary-flat.pdf](https://www.nature.com/documents/nr-reporting-summary-flat.pdf)

Life sciences study design

All studies must disclose on these points even when the disclosure is negative.

Sample size	For all experiments, we determined the sample size by following conventions in the field.
Data exclusions	No data was excluded from the analyses.
Replication	Live cell experiments were performed with two independent cell transfections. At least three individual experiments were performed using two independent purifications of dynein for biochemistry and single-molecule results, with the exception of the SEC-MALS experiments which used a single purification. All attempts at replication were successful.
Randomization	We have no data involving organisms or subjects that would require randomization.
Blinding	For the cell data (Figure 1i), samples names were removed of all signifiers before analysis.

Reporting for specific materials, systems and methods

We require information from authors about some types of materials, experimental systems and methods used in many studies. Here, indicate whether each material, system or method listed is relevant to your study. If you are not sure if a list item applies to your research, read the appropriate section before selecting a response.

Materials & experimental systems

n/a	Involved in the study
<input type="checkbox"/>	<input checked="" type="checkbox"/> Antibodies
<input type="checkbox"/>	<input checked="" type="checkbox"/> Eukaryotic cell lines
<input checked="" type="checkbox"/>	<input type="checkbox"/> Palaeontology
<input checked="" type="checkbox"/>	<input type="checkbox"/> Animals and other organisms
<input checked="" type="checkbox"/>	<input type="checkbox"/> Human research participants
<input checked="" type="checkbox"/>	<input type="checkbox"/> Clinical data

Methods

n/a	Involved in the study
<input checked="" type="checkbox"/>	<input type="checkbox"/> ChIP-seq
<input checked="" type="checkbox"/>	<input type="checkbox"/> Flow cytometry
<input checked="" type="checkbox"/>	<input type="checkbox"/> MRI-based neuroimaging

Antibodies

Antibodies used	Anti-Lis1 from Santa Cruz (catalog 374586, lot B0316) diluted 1:200; Anti-V5 from Sigma (catalog V8137, lot 128M4886V) diluted 1:2000; Anti-Beta Actin from Thermo Fisher (catalog MA515739, lot UD277186) diluted 1:2000.
Validation	The Lis1 antibody was validated as we observed signal decrease in samples treated with Lis1 siRNA in this manuscript. The anti-actin antibody is validated for western blot by Thermo Fisher for human beta actin. They also reference 174 instances of its use in the literature. The anti-V5 antibody is validated for western blot by Millipore-Sigma against the V5 tag. They also reference 84 instances of its use in the literature.

Eukaryotic cell lines

Policy information about [cell lines](#)

Cell line source(s)	U2OS cells used in this study were obtained from ATCC (HTB-96). Sf9 cells (catalog number 11496015) and Flp-In™ T-REx™ 293 Cell Line (catalog number R78007) were obtained from Thermo Fisher.
Authentication	ATCC uses morphology, karyotyping, and PCR based approaches to confirm the identity of human cell lines and to rule out both intra- and interspecies contamination. These include an assay to detect species specific variants of the cytochrome C oxidase I gene (COI analysis) to rule out inter-species contamination and short tandem repeat (STR) profiling to distinguish between individual human cell lines and rule out intra-species contamination. Sf9 and 293T cells were for protein expression and were not validated.
Mycoplasma contamination	Every new cell line we receive is tested for mycoplasma before expanding and freezing. After thawing, each cell line is tested

Mycoplasma contamination

again. Once every two months, our lab tests all growing cells for mycoplasma as well. The cells we used in our experiments were last test on 3/11/19 and did not contain contamination.

Commonly misidentified lines
(See [ICLAC](#) register)

No commonly misidentified cell lines were used